Chapter Five

Quantifying Structural Anisotropy – PMIL

5.1 Projected Mean Intercept Length

5.1.1 Introduction

The study presented in Chapter 4 showed the dominance of mechanical and hence structural anisotropy within vertebral trabecular bone and how this phenomenon may be involved in energy dissipation away from principal loading elements during trauma. Non-invasive measurement of structural anisotropy could provide important diagnostic and prognostic information about the mechanical integrity of trabecular bone. The aim of the next two chapters is to introduce two novel techniques for the assessment of structural anisotropy from projected information. The first technique (this chapter), projected mean intercept length (PMIL), bridges the gap between 3D architecture and the projected information.

To allow for comparison to other anisotropy measures, the tomographic image used in Chapter 3 (Figure 3.2) will be used throughout the next two chapters.

5.1.2 Definition of PMIL

The projected mean intercept length (PMIL) is the translation of the mean intercept length (MIL) (6) from two-dimensional (2D) data to one-dimensional (1D) projected data, as obtained in x-ray imaging. PMIL was an extension of preliminary work carried out by Reimann *et al* (1992) (3).

In this technique, 1D data are obtained by computing the Radon transform (Chapter 2, Section 2.2.8), $S(\theta, x)$, where x denotes the position within the 1D projection and θ the angle in 2D space at which the projection was taken (Figure 5.1 [B]).

The specific intercepts, defined as the number of point hits of lines with a two-phase structure's interface (1, 2, 5), is related to the Radon transform via the relationship

$$I(\theta) = \int \left| \frac{\partial S(\theta, x)}{\partial x} \right| dx \,. \qquad 5.1$$

The discrete implementation of equation 5.1 is given by

$$I(\theta) = \sum_{x=1}^{W-1} \left| S(\theta, x+1) - S(\theta, x) \right| , \qquad 5.2$$

where W is the width of the projection in pixels, S is the Radon transform of the structure at angle θ and x the position within the projection (Figures 5.1 and 5.2).

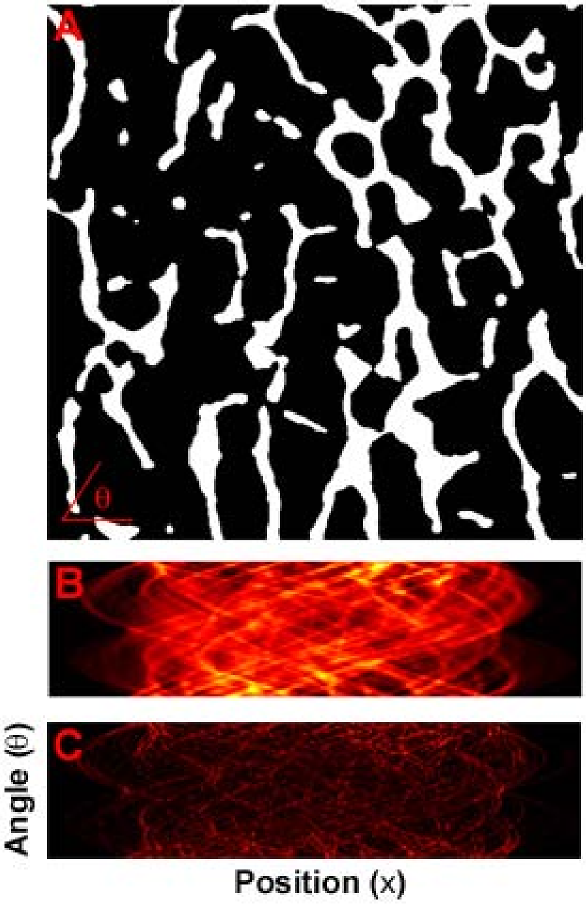

Figure 5.1 Example of a Radon transform of a binary 2D image and the PMIL. [A] Binary µCT tomograph of human trabecular bone, [B] The Radon transform of the image shown in [A] taken at 1^{o} intervals for $0^{o} \leq \theta < 180^{o}$ and [C] PMIL component, $\left|S(\theta, x+1) - S(\theta, x)\right|$, of [B]. Images [B] and [C] are shown in false colour for illustration purposes, true representations are greyscale.

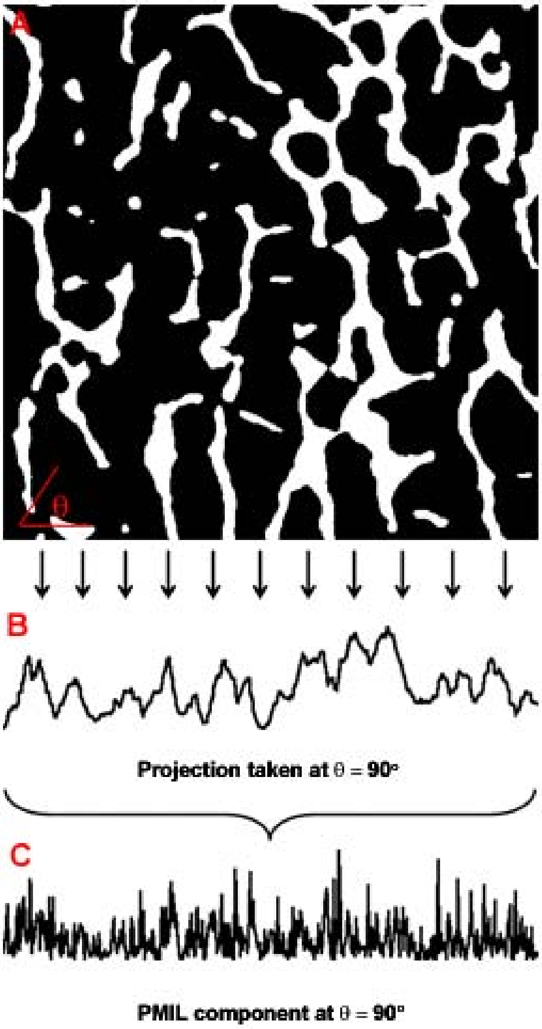

Figure 5.2 The PMIL concept. [A] Binary µCT tomograph of human trabecular bone, [B] resulting 1D Radon transform (θ = 90^o) and [C] PMIL component, $\left|S(90,x+1)-S(90,x)\right|$ (from equation 4.2), the sum of which represents the number of intercepts in the direction at which the projection was taken. The PMIL component is the absolute value of the difference of adjacent pairs of values of the projection at angle θ. For example, if the projection of an image at θ = 90^o at position $x+1$ is equal to 4, that is S(90, x+1) = 4, and the adjacent value of the projection, S(90, x) = 3, the resulting PMIL component is equal to $\left|4-3\right|$, which is equal to 1. This is then carried out on each adjacent pair of values for the length of the projection.

The structure that the PMIL represents can be visualised by taking the inverse Radon transform (Chapter 2, Section 2.2.7) of the PMIL. The PMIL of a structure represents the edge (surface) information (Figure 5.3).

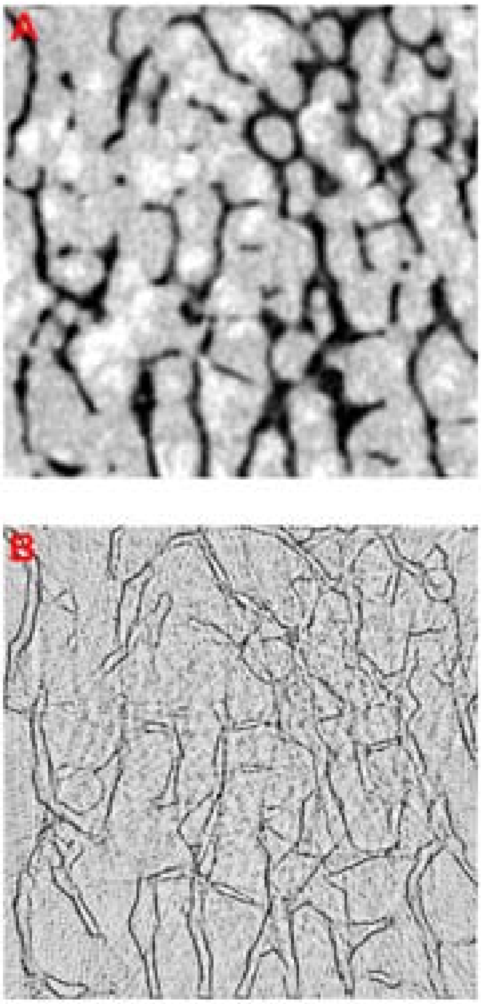

Figure 5.3 Structural representation of the PMIL. [A] Original greyscale tomograph of a human trabecular bone and [B] Inverse Radon transform of the PMIL. The inverse Radon transform allows the reconstruction of a 2D tomograph from the Radon transform of the 2D tomograph. PMIL component contains the edge (surface) information of the original tomograph [B].

Analogous to the MIL (6), representation of the mean intercept length from PMIL calculation can be found by dividing the length of the test line, in this case the width of the projections, by the number of intercepts measured. The surface distribution (or anisotropy) can be visualised in polar form in a similar manner to the MIL (Figure 5.4). The surface distribution can be represented as

$$\mathrm{PMIL}(\theta) = \frac{\mathrm{L}}{\sum_{\chi=1}^{\mathrm{W}-1} \left| \mathrm{S}(\theta, \mathrm{x}+1) - \mathrm{S}(\theta, \mathrm{x}) \right|}, \qquad 5.3$$

where L is the total length of projections in pixels.

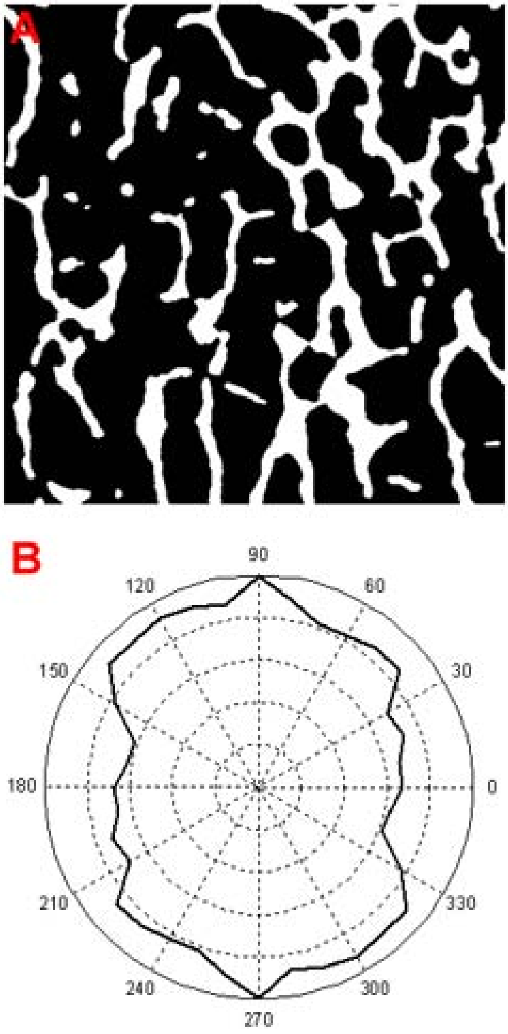

Figure 5.4 [A] Binary μCT tomograph of human trabecular bone, [B] Polar plot of the surface distribution (anisotropy) of the structure shown in [A] measured using the PMIL. The polar plot is shown in degrees.

5.1.3 Degree of Anisotropy Estimation using PMIL

As with the MIL (Chapter 3), the PMIL produces polar plots that appear elliptical (Figure 5.5). As such (and analogous to the MIL), the degree of anisotropy (DA) can be calculated using the best-fitting ellipse to the PMIL anisotropy data (Chapter 3, Section 3.7.1).

5.1.4 Total Surface Estimation using PMIL

Stereologically, the number of intercepts measured from an image using a line grid is directly related to the surface density (4, 5). By definition, the total surface is given by,

$$\frac{BS}{TV} = \frac{\pi}{2} I_L \qquad 5.4$$

Where I_L represents the mean number of intercepts measured between the line grid and the bone surface. Thus, intercept estimations made using the PMIL can be used to derive estimates of total bone surface. This concept is explored further in Section 5.2.3.

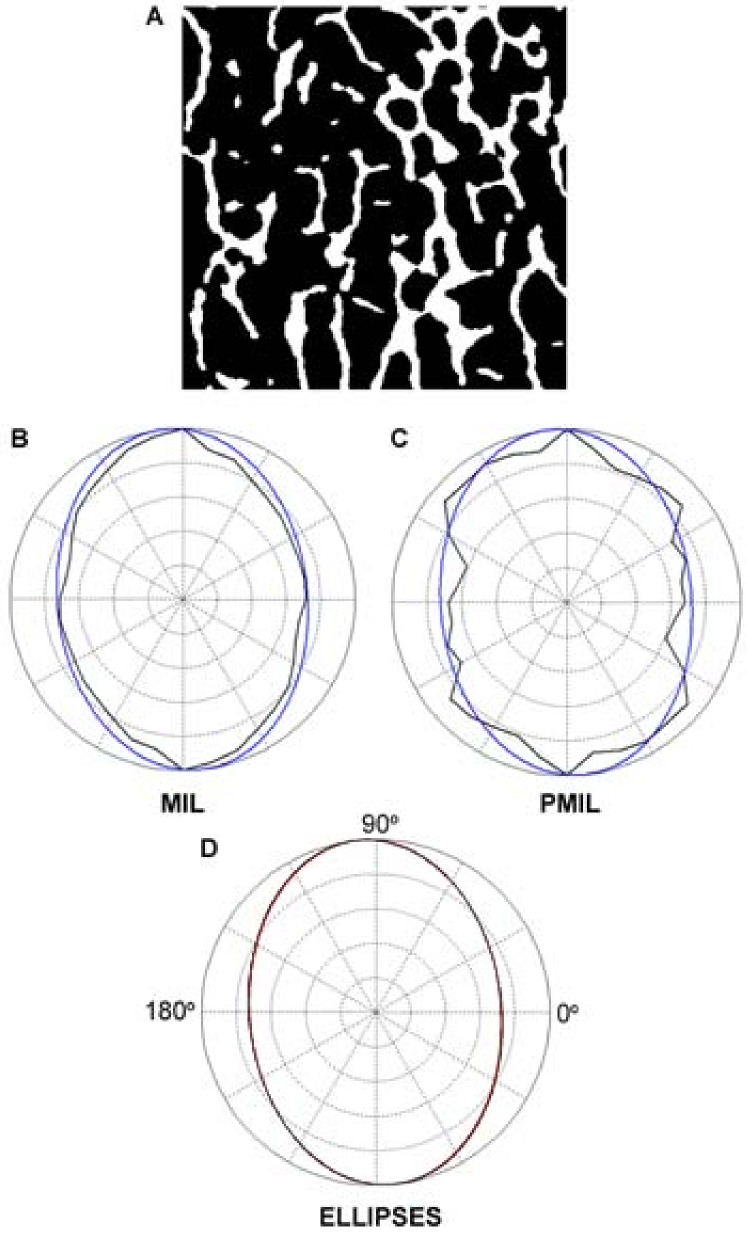

Figure 5.5 MIL versus PMIL, [A] Binary µCT tomograph of human trabecular bone, [B] MIL based surface distribution (black) with best-fitting ellipse (blue) of the structure shown in [A], [C] PMIL based surface distribution (black) with best-fitting ellipse (blue) of the structure shown in [A], [D] Ellipses from MIL (black) and PMIL (red) plotted together. Data have been have been normalised with respect to the maximum anisotropy value for illustration purposes.

5.2 Comparison of the PMIL to the MIL

5.2.1 Introduction

In Section 5.1, the PMIL concept was introduced. In the following section the relationship between the MIL and the PMIL is explored in greater detail by comparing DA and $\frac{BS}{TV}$, as computed by each measure, from real tomography data.

5.2.2 Materials & Methods

The second and third lumbar (L2 and L3, respectively) vertebral bodies from 16 individuals (8 males and 8 females), age = 59.9 ± 20.8 (mean ± standard deviation) with age ranging from 16 to 87 were collected at postmortem examination. Cubes of trabecular bone were cut from the centrum of the vertebral bodies and imaged by µCT using the protocols described in Chapter 2.

Axial tomographs obtained from reconstruction were segmented and re-sampled to coronal and sagittal tomographs. Re-sampling was carried out using custom software written in Matlab (The Mathworks). The MIL and PMIL were then measured from the 2D binary axial, coronal and sagittal tomographs from each dataset. For efficiency, every fifth tomograph from each axial, coronal and sagittal dataset was analysed, equating to an approximately 80 µm gap between slices analysed.

The DA was computed from the MIL (DA_{MIL}) and PMIL (DA_{PMIL}) anisotropy data of the mean MIL and mean PMIL anisotropy of each dataset (Chapter 3). The major orientation of the best-fitting ellipse resulting from the anisotropy data of the MIL (O_{MIL}) and PMIL (O_{PMIL}) was also computed.

The total surface ($\frac{BS}{TV}$) was calculated using both the MIL and PMIL data as described in section 5.1. In addition, $\frac{BS}{TV}$ was measured using a 3D algorithm within CTAn (Chapter 2, Section 2.2.2).

Statistical differences between measures were tested using paired t-tests, while pair-wise analyses were carried out to estimate the bias and random error between measures. Bias was defined as the mean of the difference between pair-wise measurements made using the MIL and PMIL. Random error was defined as the standard deviation of the difference between pair-wise measurements made using the MIL and PMIL. Regression analyses were used to test relationships between variables. Statistical differences in regression line slopes and intercepts were analysed using analysis of covariance (ANCOVA). All statistical analyses were performed using a combination of standard routines from SPSS (SPSS Inc.) and Matlab (The Mathworks).

5.2.3 Results

Degree of Anisotropy and Principal Orientation

For the axial and sagittal analyses, PMIL based DA was significantly larger in magnitude than the DA based on the MIL (Table 5.1). However, for the coronal analyses, the PMIL based DA was not significantly different from that of the MIL (Table 5.1).

Table 5.1 Mean ± standard deviation of DA as computed by the MIL and PMIL techniques for axial, coronal and sagittal planes. P value indicates significance. DA is dimensionless.

	MIL (-)	PMIL (-)	P
AXIAL	1.14 ± 0.10	1.18 ± 0.12	< 0.001
CORONAL	1.38 ± 0.12	1.39 ± 0.10	0.30
SAGITTAL	1.24 ± 0.11	1.26 ± 0.10	0.01

Pair-wise analyses indicated an offset (bias) between DA_{MIL} and DA_{PMIL} of less than 4% (Table 5.2).

Table 5.2 Results of pair-wise analyses for DA data based on the MIL and PMIL measures. The % column is the ratio (BIAS/DA_{MIL}) x 100, which represents the portion of DA_{MIL} that the BIAS represents. Bias and random error based DA are dimensionless.

	BIAS (-)	%	RANDOM ERROR (-)
AXIAL	0.04	3.60	0.03
CORONAL	0.01	0.83	0.06
SAGITTAL	0.02	1.26	0.04

The relationship between DA as measured by the MIL and the PMIL was computed for the axial, coronal and sagittal planes (Figure 5.6). In all three analyses, significant ($p < 0.001$) relationships were found between DA_{PMIL} and DA_{MIL}. Statistically significant ($p < 0.05$) differences were found between the slope of the regression line describing the relationship between MIL and PMIL for axial and coronal and axial and sagittal analyses. No statistically significant ($p > 0.05$) difference was observed between the slope of the regression lines of coronal and sagittal analyses. The intercept for the regression line describing the relationship between DA_{MIL} and DA_{PMIL} for the axial analyses was found to be significantly ($p < 0.05$) different to that of sagittal analyses. No significant ($p > 0.05$) difference was observed between the intercepts of the regression lines for coronal and sagittal analyses and axial and coronal analyses.

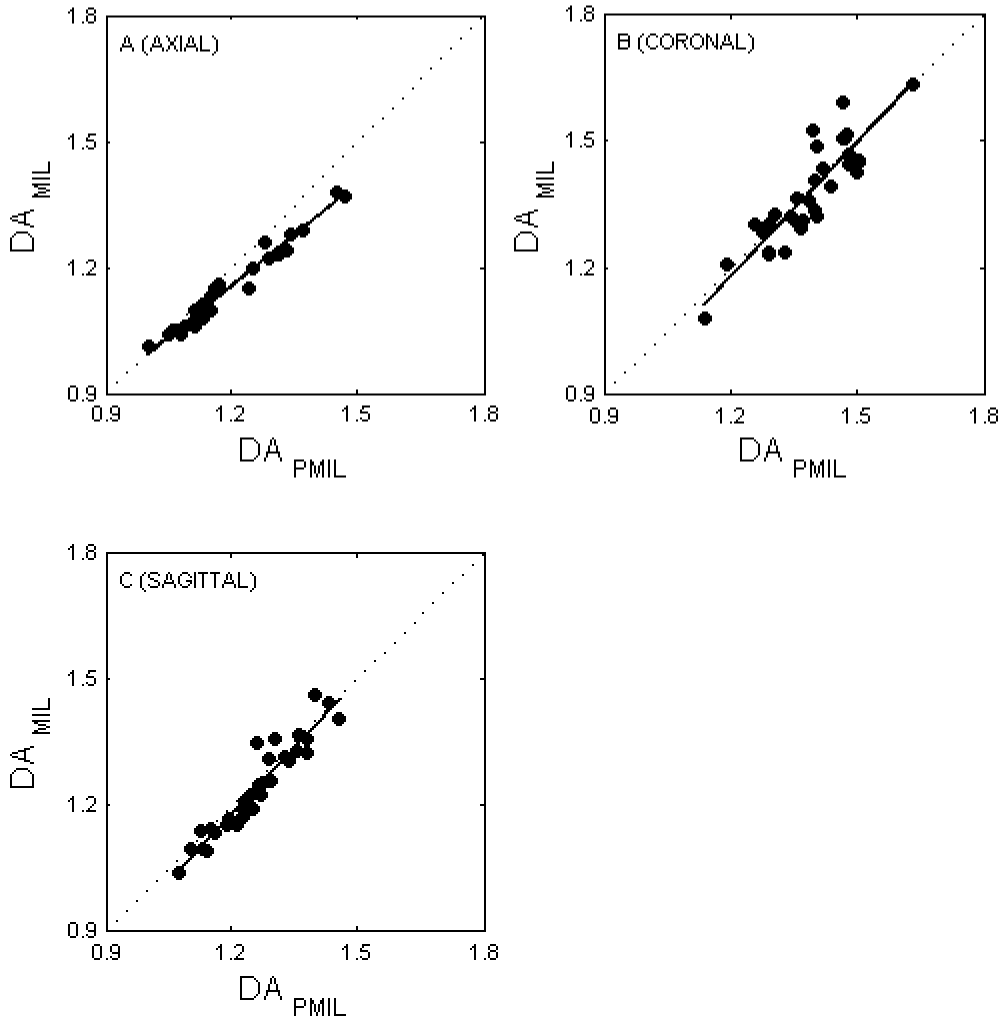

Figure 5.6 Relationship between DA as measured by MIL and PMIL from 32 lumbar vertebral trabecular bone samples. [A] Axial: $DA_{MIL} = 0.81\ DA_{PMIL} + 0.2$ ($n = 32$, $r^2 = 0.97$ and $p < 0.001$), [B] Coronal: $DA_{MIL} = 1.06\ DA_{PMIL} – 0.1$ ($n = 32$, $r^2 = 0.79$ and $p < 0.001$) and [C] Sagittal: $DA_{MIL} = 1.07\ DA_{PMIL} – 0.1$ ($n = 32$, $r^2 = 0.90$ and $p < 0.001$). Broken lines represent lines of identity.

There was no significant difference in the principal orientation (O) as measured by the MIL and PMIL for axial, coronal or sagittal analyses (Table 5.3).

Table 5.3 Mean ± standard deviation of O as computed by the MIL and PMIL for axial, coronal and sagittal planes. P value indicates significance. O has units of degrees.

	MIL (DEG.)	PMIL (DEG.)	P
AXIAL	93.1 ± 33.1	96.4 ± 29.3	0.26
CORONAL	91.7 ± 6.7	91.6 ± 6.3	0.61
SAGITTAL	87.6 ± 14.2	87.5 ± 13.8	0.92

Pair-wise analyses, similar to those used for the DA, indicated that the offset (bias) was less that 5% for the axial analyses and less that 0.2% for the more anisotropic coronal and sagittal analyses (Table 5.4)

Table 5.4 Results of pair-wise analyses of O data based on the MIL and PMIL measures. The % column is the ratio (BIAS/O_{MIL}) x 100, which represents the portion of O_{MIL} that the BIAS represents. Bias and random error have units of degrees.

	BIAS (DEG.)	%	RANDOM ERROR (DEG.)
AXIAL	3.7	4.0	18.4
CORONAL	0.1	0.1	1.2
SAGITTAL	0.0	0.0	2.0

The relationship between O, as measured from the best-fitting ellipse to the MIL and PMIL, data was computed for axial, coronal and sagittal planes (Figure 5.7). No statistically significant (p >

0.05) differences were found between the slopes or the intercepts of the regression lines describing the relationships between O_{MIL} and O_{PMIL} for axial, coronal or sagittal analyses.

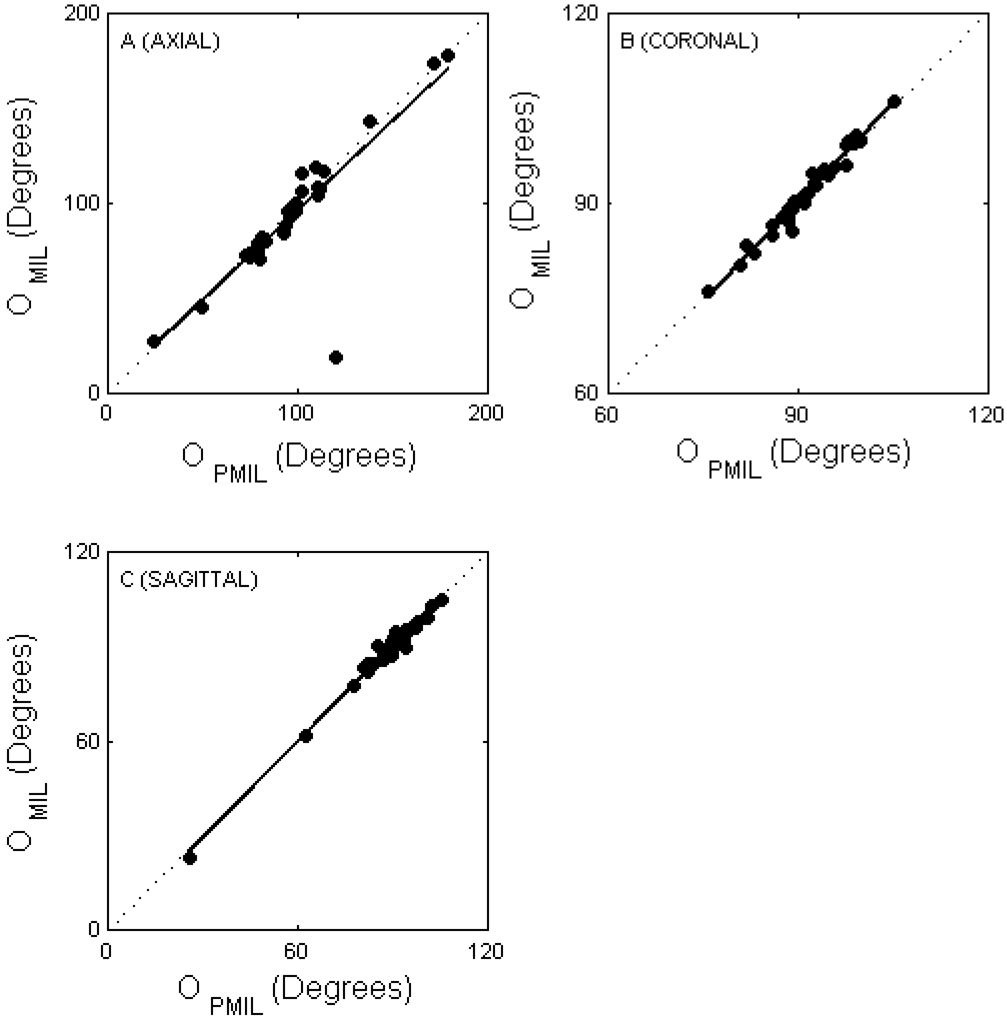

Figure 5.7 Relationship between orientation as measured by MIL and PMIL from 32 lumbar vertebral trabecular bone samples. [A] Axial: $O_{MIL} = 0.94\ O_{PMIL} + 1.9$ ($n = 32$, $r^2 = 0.70$ and $p < 0.001$), [B] Coronal: $O_{MIL} = 1.04\ O_{PMIL} – 3.8$ ($n = 32$, $r^2 = 0.97$ and $p < 0.001$) and [C] Sagittal: $O_{MIL} = 1.02\ DA_{PMIL} – 1.5$ ($n = 32$, $r^2 = 0.98$ and $p < 0.001$). Broken lines represent lines of identity.

Total Bone Surface – MIL & PMIL

In axial, coronal and sagittal analyses, MIL based $\frac{BS}{TV}$ was significantly smaller in magnitude than PMIL based $\frac{BS}{TV}$ (Table 5.5).

Table 5.5 Mean ± standard deviation of $\frac{BS}{TV}$ as computed by the MIL and PMIL techniques for axial, coronal and sagittal planes. P value indicates significance. BS/TV has units of mm^2/mm^3.

	MIL (mm^2/mm^3)	PMIL (mm^2/mm^3)	P
AXIAL	1.81 ± 0.61	2.18 ± 0.48	< 0.001
CORONAL	1.61 ± 0.48	2.04 ± 0.40	< 0.001
SAGITTAL	1.52 ± 0.42	2.01 ± 0.36	< 0.001

Pair-wise analyses indicated that the offset (bias) between MIL and PMIL based $\frac{BS}{TV}$ across axial, coronal and sagittal analyses was, on average, 26% (Table 5.6).

Table 5.6 Results of pair-wise analyses of estimates of total bone surface based on the MIL and PMIL measures. The % column is the ratio (BIAS/BS/TV$_{MIL}$) x 100, which represents the portion of BS/TV$_{MIL}$ that the BIAS represents. Bias and random error have units of mm^2/ mm^3.

	BIAS (mm^2/mm^3)	%	RANDOM ERROR (mm^2/mm^3)
AXIAL	0.36	20	0.15
CORONAL	0.43	27	0.10
SAGITTAL	0.49	32	0.08

The relationship between $\frac{\text{BS}}{\text{TV}}$ as measured by MIL and PMIL was computed for the axial, coronal and sagittal planes (Figure 5.8). Statistically significant ($p < 0.001$) and strong relationships ($r^2 = 0.98$) relationships were observed across all analyses. A statistically significant ($p < 0.05$) difference was found between the slopes of the regression lines describing the relationship between MIL and PMIL based $\frac{\text{BS}}{\text{TV}}$ for axial and sagittal analyses. No such difference ($p > 0.05$) was found between coronal and any other analyses.

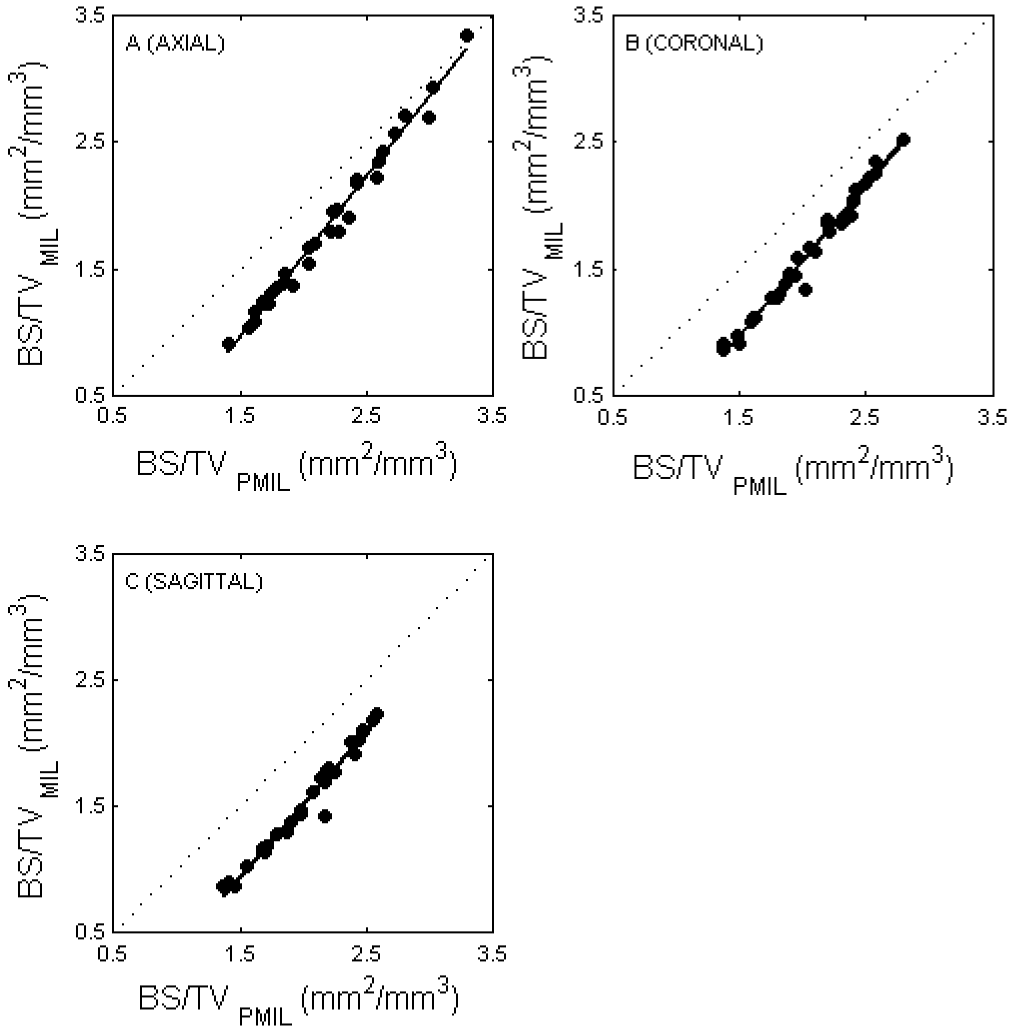

Figure 5.8 Relationship between total bone surface (BS/TV) as measured by MIL and PMIL from 32 lumbar vertebral trabecular bone samples. [A] Axial: BS/TV_{MIL} = 1.3 BS/TV_{PMIL} – 0.9, (n = 32, $r^2 = 0.98$ and $p < 0.001$), [B] Coronal: BS/TV_{MIL} = 1.2 BS/TV_{PMIL} – 0.8 (n = 32, $r^2 = 0.98$ and $p < 0.001$) and [C] Sagittal plane: BS/TV_{MIL} = 1.1 BS/TV_{PMIL} – 0.8 (n = 32, $r^2 = 0.98$ and $p < 0.001$). Broken line represents line of identity.

Total Bone Surface – 2D & 3D

Relationships between 2D measures of $\frac{BS}{TV}$ from axial, coronal and sagittal analyses and 3D $\frac{BS}{TV}$ ($\frac{BS}{TV}_{3D}$), measured by µCT were investigated. For axial, coronal and sagittal analyses, $\frac{BS}{TV}_{MIL}$ was significantly smaller in magnitude than $\frac{BS}{TV}_{3D}$ (Table 5.7).

Table 5.7 Mean ± standard deviation of $\frac{BS}{TV}$ as computed in 3D and 2D by the MIL for axial, coronal and sagittal planes. P value indicates significance. BS/TV has units of mm^2/mm^3.

	3D (mm^2/mm^3)	MIL (mm^2/mm^3)	P
AXIAL	2.38 ± 0.63	1.81 ± 0.61	< 0.001
CORONAL	2.38 ± 0.63	1.61 ± 0.48	< 0.001
SAGITTAL	2.38 ± 0.63	1.52 ± 0.42	< 0.001

Pair-wise analyses indicated that $\frac{BS}{TV}_{MIL}$ was, on average, $\frac{3}{4}$ the magnitude of $\frac{BS}{TV}_{3D}$ (Table 5.8).

Table 5.8 Results of pair-wise analyses of BS/TV data based on the 2D MIL and 3D µCT measures. The % column is the ratio (BIAS/BS/TV_{3D}) x 100, which represents the portion of BS/TV_{3D} that the BIAS represents. Bias and random error have units of mm^2/mm^3.

	BIAS (mm^2/mm^3)	%	RANDOM ERROR (mm^2/mm^3)
AXIAL	0.57	24	0.40
CORONAL	0.77	33	0.21
SAGITTAL	0.86	36	0.25

The relationship between $\frac{BS}{TV}_{3D}$ and $\frac{BS}{TV}_{MIL}$ was computed for the axial, coronal and sagittal planes (Figure 5.9, solid circles). Statistically significant ($p < 0.001$) relationships were observed for all analyses. Significant ($p < 0.05$) differences were found between the slope of the regression line describing the relationship between $\frac{BS}{TV}_{3D}$ and $\frac{BS}{TV}_{MIL}$ for axial analyses and both coronal and sagittal analyses. No significant difference ($p > 0.05$) was observed between the slopes of coronal and sagittal analyses. Significant ($p < 0.05$) differences were found between the intercept of the regression line describing the relationship between $\frac{BS}{TV}_{3D}$ and $\frac{BS}{TV}_{MIL}$ for axial analyses and both coronal and sagittal analyses, while no such difference was observed between coronal and sagittal analyses.

Similar analyses were carried out for the PMIL. For axial, coronal and sagittal analyses, $\frac{BS}{TV}_{PMIL}$ was significantly smaller in magnitude than $\frac{BS}{TV}_{3D}$ (Table 5.9).

Table 5.9 Mean ± standard deviation of $\frac{BS}{TV}$ as computed in 3D and 2D by the PMIL for axial, coronal and sagittal planes. P value indicates significance. BS/TV has units of mm^2/mm^3.

	3D (mm^2/mm^3)	PMIL (mm^2/mm^3)	P
AXIAL	2.38 ± 0.63	2.18 ± 0.48	< 0.001
CORONAL	2.38 ± 0.63	2.04 ± 0.40	< 0.001
SAGITTAL	2.38 ± 0.63	2.01 ± 0.36	< 0.001

Pair-wise analyses indicated that $\frac{BS}{TV}_{PMIL}$ was, on average, approximately 12% smaller than $\frac{BS}{TV}_{3D}$ (Table 5.10).

Table 5.10 Results of pair-wise analyses of BS/TV data based on the PMIL and 3D measures. The % column is the ratio ($BIAS/BS/TV_{3D}$) x 100, which represents the portion of BS/TV_{3D} that the BIAS represents. Bias and random error have units of mm^2/ mm^3.

	BIAS (mm^2/mm^3)	%	RANDOM ERROR (mm^2/mm^3)
AXIAL	0.20	8	0.41
CORONAL	0.34	14	0.28
SAGITTAL	0.37	15	0.31

The relationship between $\frac{BS}{TV}_{3D}$ and $\frac{BS}{TV}_{PMIL}$ was computed for the axial, coronal and sagittal planes (Figure 5.10, empty circles). Relationships between slopes and intercepts were similar to those of MIL based analyses. Significant ($p < 0.05$) differences were found between the slope of the regression lines describing the relationship between $\frac{BS}{TV}_{3D}$ and $\frac{BS}{TV}_{PMIL}$ for axial analyses and both coronal and sagittal analyses. No significant difference was observed between the slopes of coronal and sagittal analyses. Similarly, significant differences were found between the intercept of the regression line describing the relationship between $\frac{BS}{TV}_{3D}$ and $\frac{BS}{TV}_{PMIL}$ for axial analyses and both coronal and sagittal analyses, while no such difference ($p > 0.05$) was observed between coronal and sagittal analyses.

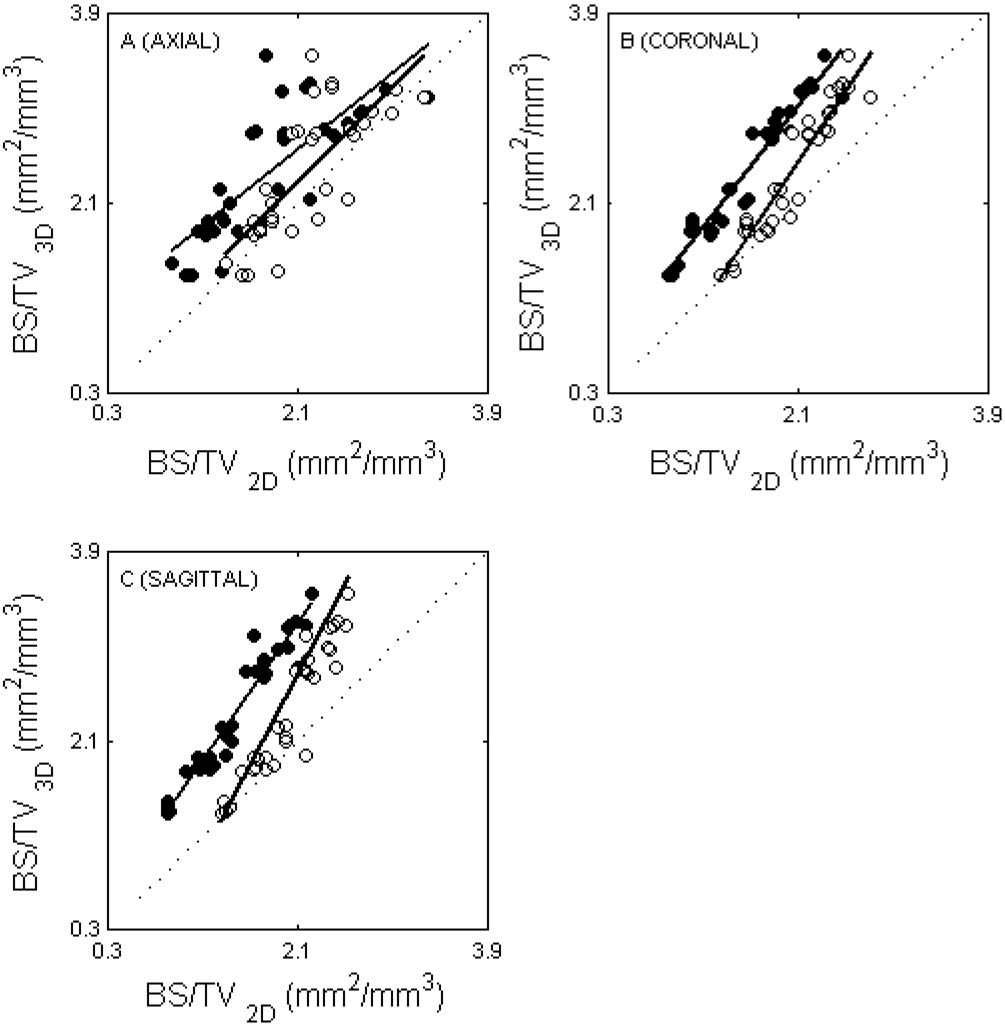

Figure 5.9 Relationship between BS/TV_{3D} and BS/TV_{2D} as measured by MIL (solid) and PMIL (empty). [A] Axial: $\frac{BS}{TV_{3D}} = 0.8 \times \left(\frac{BS}{TV_{MIL}}\right) + 0.92$ (n = 32, r^2 = 62 and $p < 0.001$), $\frac{BS}{TV_{3D}} = 0.9 \times \left(\frac{BS}{TV_{PMIL}}\right) - 0.21$ (n = 32, r^2 = 0.58 and $p < 0.001$),

[B] Coronal: $\frac{BS}{TV_{3D}} = 1.3 \times \left(\frac{BS}{TV_{MIL}}\right) + 0.33$ (n = 32, r^2 = 0.93 and $p < 0.001$), $\frac{BS}{TV_{3D}} = 1.5 \times \left(\frac{BS}{TV_{PMIL}}\right) - 0.68$ (n = 32, r^2 = 0.90 and $p < 0.001$),

[C] Sagittal: $\frac{BS}{TV_{3D}} = 1.4 \times \left(\frac{BS}{TV_{MIL}}\right) + 0.18$ (n = 32, r^2 = 0.93 and $p < 0.001$), $\frac{BS}{TV_{3D}} = 1.6 \times \left(\frac{BS}{TV_{PMIL}}\right) - 0.89$ (n = 32, r^2 = 0.89 and $p < 0.001$). Broken line represents line of identity.

5.2.4 Discussion

PMIL was capable of extracting the same information about DA from the projection as the MIL was from the tomographic data. Comparison between MIL and PMIL, showed that the DA was significantly larger in magnitude for the PMIL than the MIL for both sagittal and axial, but not for the coronal analyses. While there were differences, the amount of offset (bias) was less than 4% of the referent (DA_{MIL}) in each case, with quite low and consistent random error between measures. This is further supported by the strong linear relationship between DA_{MIL} and DA_{PMIL} (Figure 5.6), coupled with the fact that the principal orientations measured by each measure were not significantly different from one another.

Strong linear relationships between $\frac{BS}{TV}_{MIL}$ and $\frac{BS}{TV}_{PMIL}$ (Figures 5.8) and $\frac{BS}{TV}_{2D}$ (MIL and PMIL) and $\frac{BS}{TV}_{3D}$ measures (Figure 5.9) indicate that the PMIL was capable of extracting total surface information from the projection of the structure. $\frac{BS}{TV}_{MIL}$ was significantly smaller in magnitude that $\frac{BS}{TV}_{PMIL}$, with $\frac{BS}{TV}_{PMIL}$ biased, on average, by 26% in relation to the referent ($\frac{BS}{TV}_{MIL}$). This, in combination with the strong linear relationships between measures indicates that the two measures are related by an affine transformation. That is, $\frac{BS}{TV}_{PMIL}$ needs to be scaled by a constant to get a magnitude equivalent of $\frac{BS}{TV}_{MIL}$. This is further supported by the findings relating to $\frac{BS}{TV}_{3D}$, where both MIL and PMIL measures were lower in magnitude than the 3D measure, but strongly correlated. This, again, points toward an affine transform between the measures and the referent.

This chapter has shown that the PMIL can provide the same information about degree of anisotropy and total bone surface from projections of a structure as the MIL can from tomographic data. This work presents the framework for the assessment of these parameters from non-invasive modalities such as peripheral quantitative computed tomography and plain x-rays. In Appendix B and Chapter 7, the explanatory value of microarchitectural parameters measured using the PMIL are explored further.

In the next chapter, a second technique for the assessment of structural anisotropy is introduced that is more sensitive to structural anisotropy than the PMIL.

References

1. Harrigan, T. P., and Mann, R. W. Characterization of Microsturctural Anisotropy in Orthotropic Materials Using a Second Rank Tensor. Journal of Material Science 19:761 - 767; 1984.
2. Kanatani, K. Measurement of Particle Orientation Distribution by a Stereological Method. Part. Charact. 2:31 - 37; 1985.
3. Reimann, D. A., Fyhrie, D.P., Fazzalari, N.L., Schaffler, M.B. Trabecular Bone Morphometry by Volume Projection. 38th Annual Meeting, Orthopaedic Research Society, pp. 561. Washington, D.C.; 1992.
4. Russ, J. C., and Dehoff, R. T. Practical Stereology. New York: Plenum Publishers; 2000.
5. Snyder, B. D. Anisotropic Structure-Property Relations for Trabecular Bone. Bioengineering, pp. 260: Univeristy of Pennsylvania; 1991.
6. Whitehouse, W. J. The quantitative morphology of anisotropic trabecular bone. J Microsc 101 Pt 2:153-68; 1974.

Chapter Six

Quantifying Structural Anisotropy – LPD

6.1 Line Projection Deviation

6.1.1 Introduction

The line projection deviation (LPD) is based on the measurement of structural alignment from the Radon transform (Chapter 2, Section 2.2.8). The LPD is defined as the standard deviation of the projection obtained from the image. This method is based on the principle that the projection of aligned structures produces a peak in the projection relative to the background. Unlike the MIL (Chapter 3) and PMIL (Chapter 5), the LPD provides more detailed information on structural alignment, however like the LFD (Chapter 3) it has no direct relationship to stereology (2).

6.1.2 Definition of LPD

If projections are taken from multiple views of an aligned structure, the standard deviation of the projection at each view will vary according to the structural alignment. Taking projections of an image, within the same plane of the image, in multiple orientations, results in the Radon transform, $S(\theta, x)$, where x denotes position within the 1D projection and θ the angle in 2D space at which the projection was taken (4) (Chapter 2, Section 2.2.7). The LPD is then defined as the standard deviation of $S(\theta, x)$ along x for fixed angles θ. Figure 6.1 illustrates the LPD graphically.

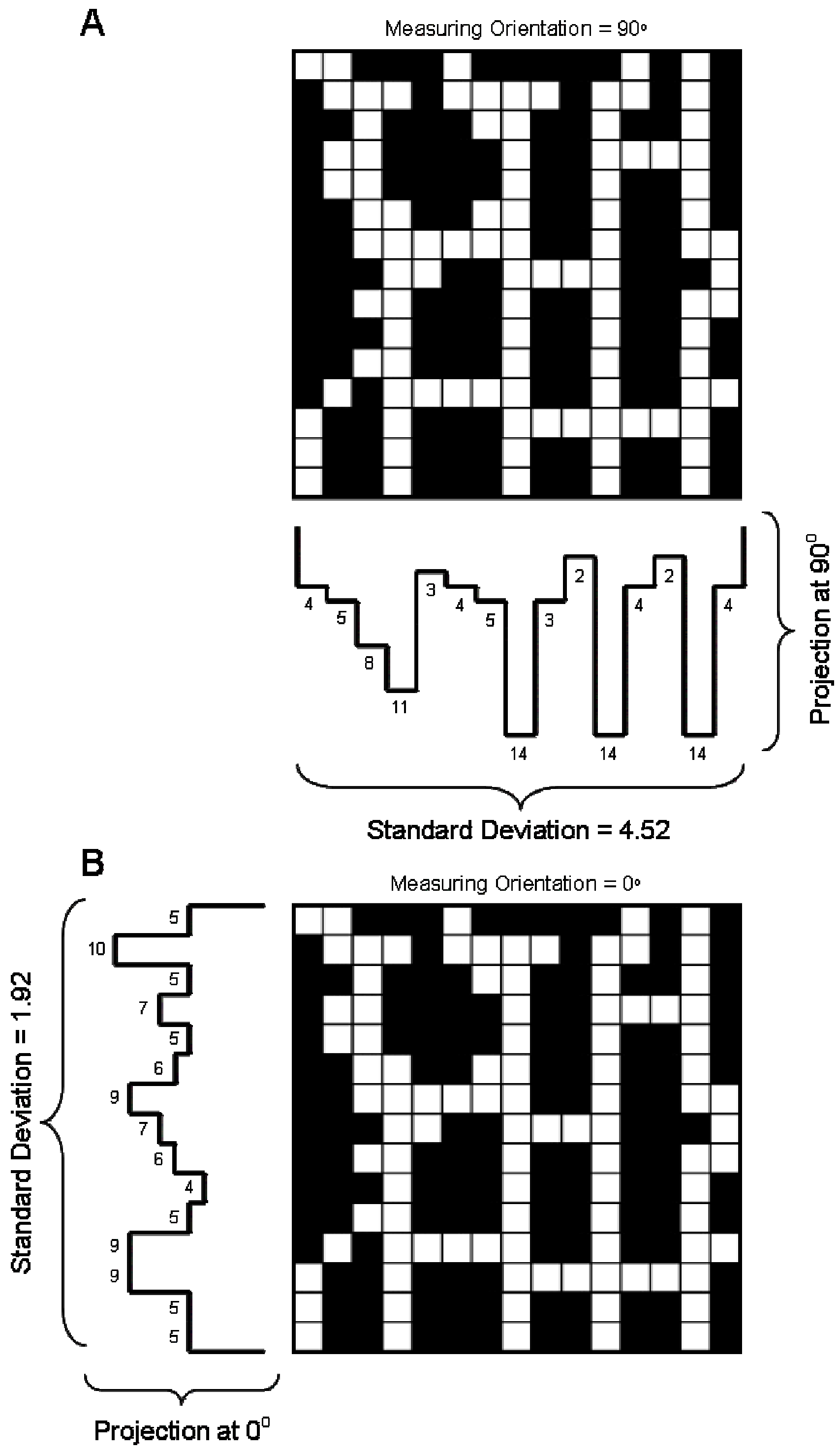

Figure 6.1 The LPD depicted graphically. [A] With the measuring orientation set at $\theta = 90^{o}$, up and down the page, the standard deviation of the projection is greater ($\sigma = 4.52$) than that when the measuring orientation is at $\theta = 0^{o}$, across the page [B] ($\sigma = 1.92$), thus quantifying greater structural alignment at 90^{o} than at 0^{o}.

6.1.3 Degree of Anisotropy Estimation Using LPD

Similar to other measures of anisotropy (2), values of LPD measured at orientation θ are the same as the values measured at orientation $\theta \pm n\pi$ for any n. Thus, when measured at equal intervals, a polar plot depicting the textural anisotropy of the image can be generated (Figure 6.2). The degree of anisotropy (DA) can then be computed as previously described (Chapter 3 Section 3.7.1) (Figure 6.3).

As a textural descriptor, the LPD measures relative differences and unlike the MIL (5) and LFD (3), is not restricted to binary images. The LPD can measure the textural anisotropy of any structure represented in a greyscale image. In cases where there are high contrast greyscale images of two-phase structures (e.g. µCT tomograph of trabecular bone), the textural anisotropy measured by LPD will be very similar to that measured from the binary equivalent, with any discrepancies likely to be due to the segmentation process (Figure 6.4 and Section 6.2).

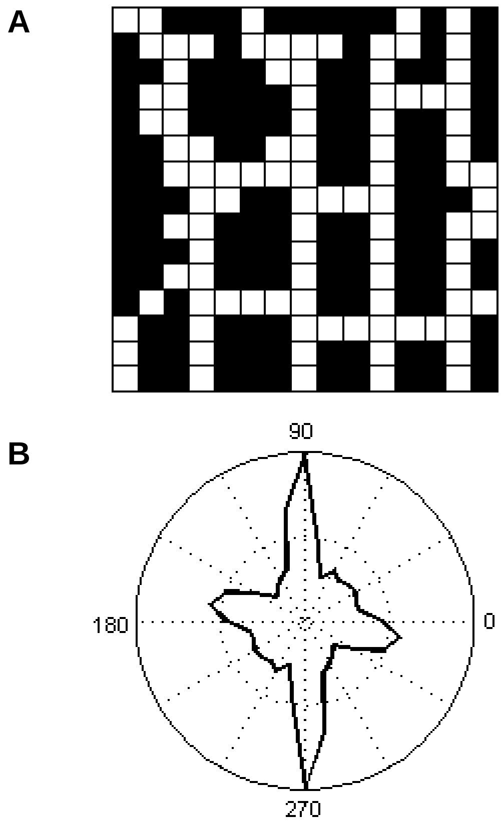

Figure 6.2. Textural anisotropy of the structure shown [A], measured at 10^{o} intervals using the LPD, plotted in polar form [B].

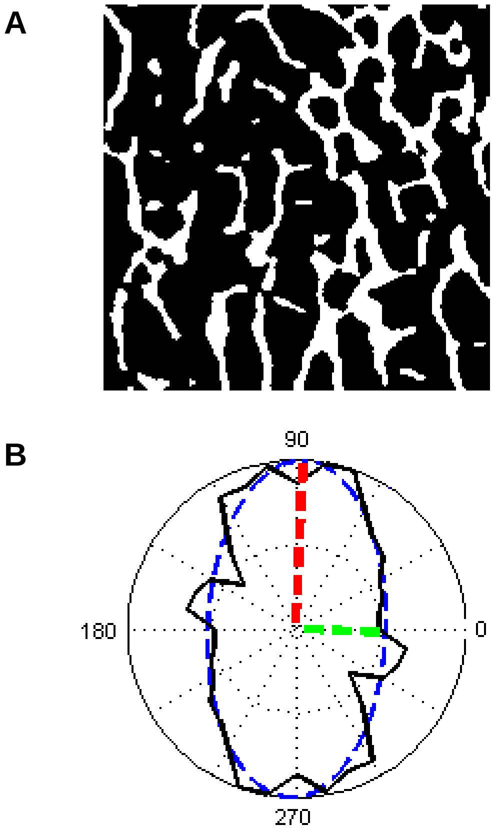

Figure 6.3 Example illustrating structural anisotropy measured using the LPD. [A] Binary µCT tomograph of human vertebral trabecular bone, [B] LPD based anisotropy (solid black), best-fitting ellipse (broken blue), the major (broken red) and minor (broken green) axes of the best fitting ellipse. Data have been normalised with respect to the maximum for illustration purposes.

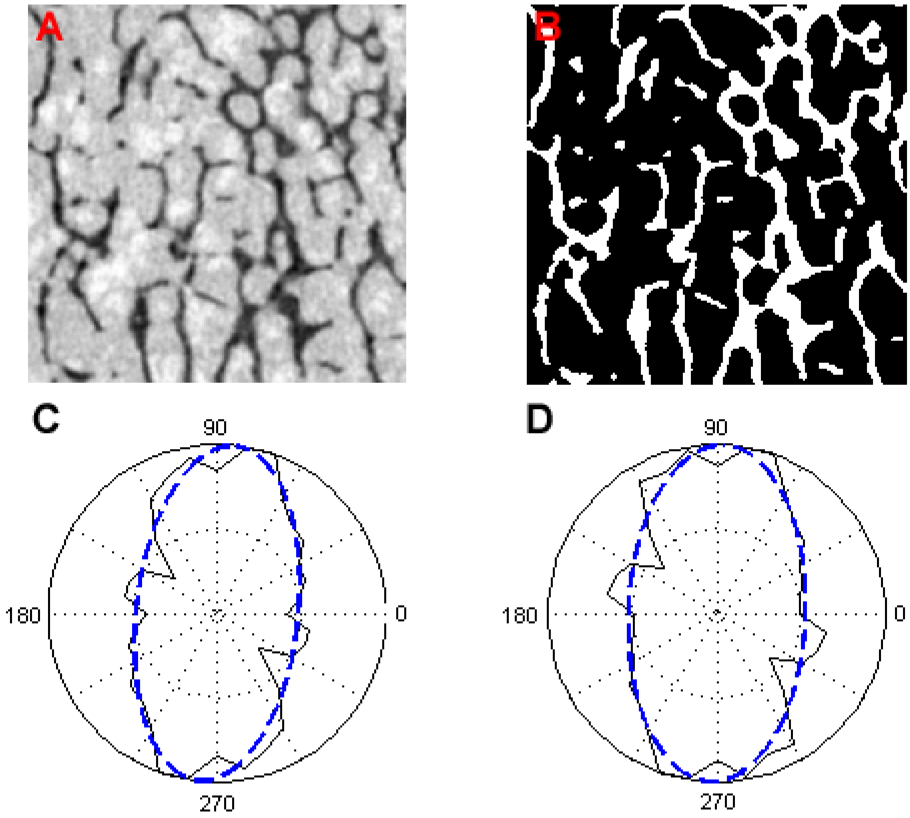

Figure 6.4 [A] Greyscale µCT tomograph of human vertebral trabecular bone, [B] Segmented binary representation of the tomograph shown in [A], [C] Textural anisotropy measured using the LPD on the greyscale image shown in [A] (black) with the best-fitting ellipse (blue), [D] Textural anisotropy measured using the LPD on the binary image shown in [B] (black) with the best-fitting ellipse (blue). Data have been normalised with respect to the maximum for illustration purposes.

6.2 Comparison of LPD to the LFD

6.2.1 Introduction

In this section, the LPD is explored in greater detail by comparisons between the LPD and the LFD (Chapter 3).

6.2.2 Materials & Methods

The tomographs used in the study described in Section 5.2.2 of Chapter 5 were also used to analyse properties of the LFD and LPD. Briefly, 32 L2 and L3 cubes of vertebral bone where imaged using µCT. Axial tomographs obtained from reconstruction were segmented and re-sampled to coronal and sagittal tomographs. The LFD and LPD were then measured from the 2D binary axial, coronal and sagittal tomographs from each dataset.

The DA was computed from the LFD (DA_{LFD}) and LPD (DA_{LPD}) anisotropy data of each dataset. The major orientation of the best-fitting ellipse resulting from the anisotropy data of the LFD (O_{LFD}) and LPD (O_{LPD}) were also computed. Comparisons between DA_{LFD} and DA_{LPD} and O_{LFD} and O_{LPD} were made.

Statistical differences between measures were tested using paired t-tests, while pair-wise analyses were carried out to estimate the bias and random error between measures. Bias was defined as the mean of the difference between pair-wise measurements made using the LFD and LPD. Random error was defined as the standard deviation of the difference between pair-wise measurements made using the LFD and LPD. Regression analyses were used to test relationships between variables. Statistical differences in regression line slopes and intercepts were analysed using analysis of covariance (ANCOVA). Cases exerting undue influence (outliers) on the relationships were identified and excluded using Cook's distance (1). All statistical analyses were performed using a combination of standard routines within SPSS (SPSS Inc.) and Matlab (The Mathworks).

6.2.3 Results

Degree of Anisotropy

For axial, coronal and sagittal analyses, there was no significant difference between DA_{LFD} and DA_{LPD} (Table 6.1).

Table 6.1 Mean ± standard deviation of DA as computed by the LFD and LPD measures for axial, coronal and sagittal planes. P value indicates significance. DA is dimensionless.

	LFD (-)	LPD (-)	P
AXIAL	1.21 ± 0.12	1.21 ± 0.12	0.92
CORONAL	1.74 ± 0.31	1.78 ± 0.31	0.10
SAGITTAL	1.49 ± 0.25	1.51 ± 0.23	0.07

Pair-wise analyses indicated an offset between DA_{LFD} and DA_{LPD} of less than 2.1% (Table 6.2).

Table 6.2 Results of pair-wise analyses for DA based on the LFD and LPD measures. The % column is the ratio (BIAS/DA_{LFD}) x 100, which represents the portion of DA_{LFD} that the BIAS represents. Bias and random error based DA are dimensionless.

	BIAS (-)	%	RANDOM ERROR (-)
AXIAL	0.01	0.91	0.07
CORONAL	0.04	2.07	0.11
SAGITTAL	0.02	1.54	0.07

The linear relationship between DA_{LFD} and DA_{LPD} was computed for the axial, coronal and sagittal planes (Figure 6.5). Significant relationships ($p < 0.001$) were identified for all analyses ($r^2 \in [0.75, 0.90]$). No significant differences ($p > 0.05$) were found between the slopes or intercepts of regression lines describing the relationship between DA_{LFD} and DA_{LPD} for axial, coronal or sagittal analyses.

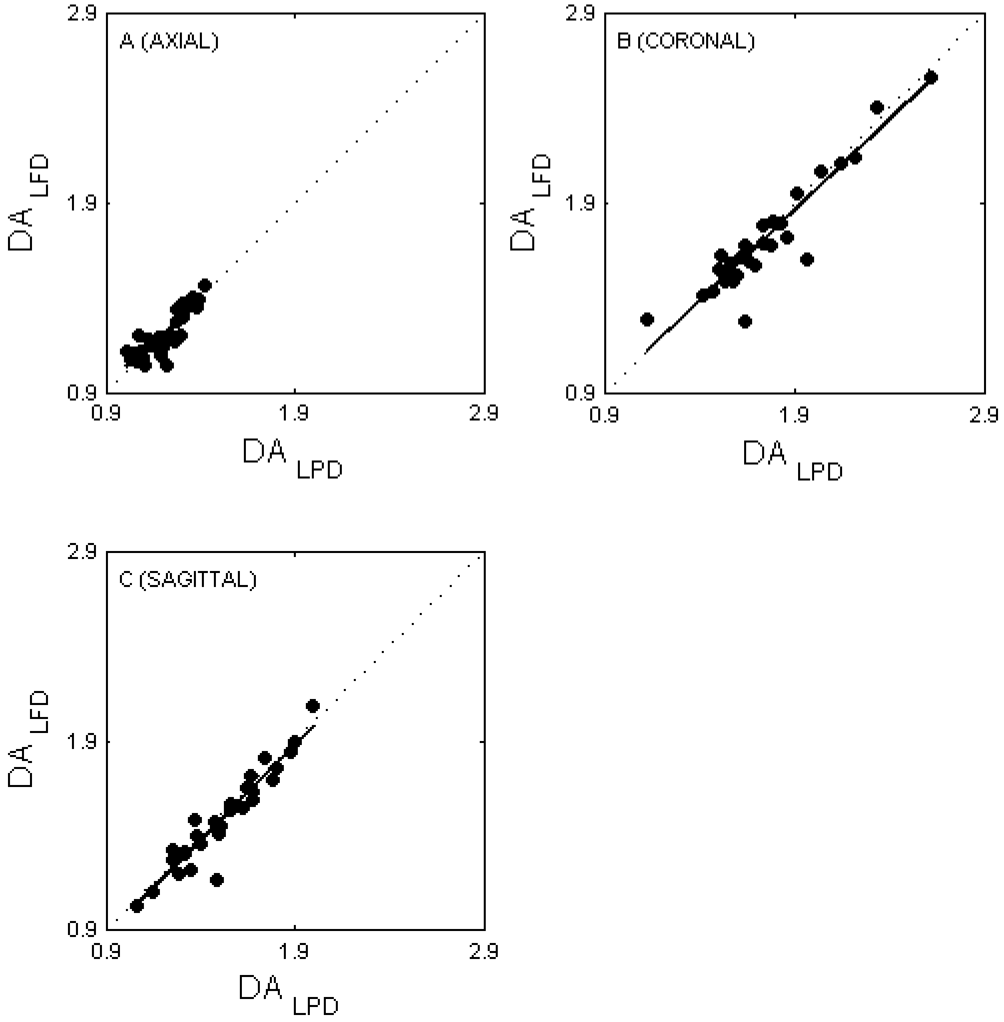

Figure 6.5 Linear relationships between DA as measured by the LFD and LPD. [A] Axial: $DA_{LFD} = 0.88(DA_{LPD}) + 0.14$ (n = 32, r^2 = 0.75 and $p < 0.001$); [B] Coronal: $DA_{LFD} = 0.95(DA_{LPD}) + 0.05$ (n = 32, r^2 = 0.88 and $p < 0.001$) and [C] Sagittal: $DA_{LFD} = 1.01(DA_{LPD}) + 0.04$ (n = 32, r^2 = 0.90 and $p < 0.001$). Dotted lines represent lines of identity.

Principal Orientation

Two axial and one sagittal data point were identified as outliers and excluded based on Cook's distance (Figure 6.6). For axial (n = 30), coronal (n = 32) and sagittal (n = 31) analyses, there was no significant difference between O_{LFD} and O_{LPD} (Table 6.3).

Table 6.3 Mean ± standard deviation of orientation as computed by the LFD and LPD measures for axial (n = 30), coronal (n = 32) and sagittal (n = 31) planes. P value indicates significance. Orientation has units of degrees.

	LFD (DEG.)	LPD (DEG.)	P
AXIAL	94.4 ± 31.0	93.5 ± 31.6	0.69
CORONAL	91.6 ± 15.3	92.3 ± 15.0	0.23
SAGITTAL	84.8 ± 9.9	84.4 ± 13.3	0.76

Pair-wise analyses indicated an offset (bias) between O_{LFD} and O_{LPD} of less than 1% (Table 6.4).

Table 6.4 Results of pair-wise analyses for orientation based on the LFD and LPD measures. The % column is the ratio (BIAS/O_{LFD}) x 100, which represents the portion of O_{LFD} that the BIAS represents. Bias and random error have units of degrees.

	BIAS (DEG.)	%	RANDOM ERROR (DEG.)
AXIAL	0.90	0.95	12.20
CORONAL	0.72	0.79	3.30
SAGITTAL	0.35	0.41	6.30

The linear relationship between O_{LFD} and O_{LPD} was computed for the axial, coronal and sagittal analyses (Figure 6.6). Significant ($p < 0.05$) and strong ($r^2 \in [0.79, 0.95]$) relationships were found for all analyses. Similar to the DA, no significant differences ($p > 0.05$) were found between the slopes or intercepts of regression lines describing the relationship between O_{LFD} and O_{LPD} for axial, coronal or sagittal analyses.

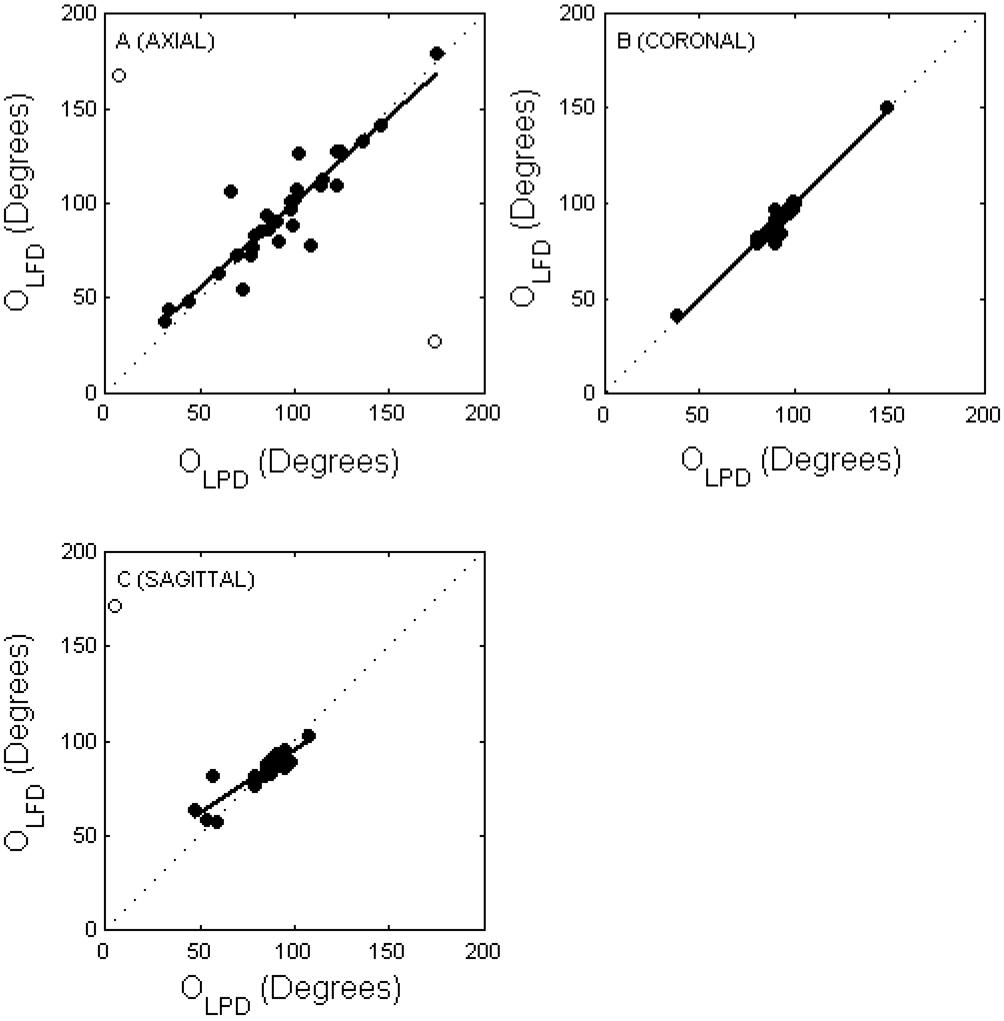

Figure 6.6 Linear relationships between orientation as measured by the LFD (O_{LFD}) and LPD (O_{LPD}). [A] Axial (excluding 2 outliers; open circles): $O_{LFD} = 0.91(O_{LPD}) + 9.67$ (n = 30, $r^2 = 0.85$, $p < 0.001$); [B] Coronal: $O_{LFD} = 0.99(O_{LPD}) - 0.09$ (n = 32, $r^2 = 0.95$, $p < 0.001$) and [C] Sagittal (excluding 1 outlier; open circle): $O_{LFD} = 0.66(O_{LPD}) + 28.93$ (n = 31, $r^2 = 0.79$, $p < 0.001$). Dotted lines represent lines of identity.

6.2.4 Discussion

The LPD was capable of extracting the same architectural information from the projection of a structure as the LFD was from the tomograph of that structure. No significant differences were found between measures of DA or orientation between LFD and LPD. Pairwise analyses identified a typical offset of less than 2% between the LFD and LPD, while regression analyses showed very strong and linear relationships between the two techniques. Thus, the LPD technique is capable of assessing structural anisotropy from projections.

Outliers were identified in orientation measurements and excluded based on Cook's distance (1). In comparisons between principal orientation as measured from the best fitting ellipse, two axial and one sagittal data point were identified as being influential outliers (Figure 6.6). The identification of these outliers was not surprising given that differences between LFD and LPD can result in quite different orientation values from the ellipse fitting. Thus, the outliers identified in the present study are likely due to ellipse fitting differences than differences resulting from the original data (Figure 6.7).

Embedded in these results is also the fact that the principal orientation carries less significant meaning in isotropic structures, such as those of the axial plane, than the more aligned (anisotropic) structures, such as the coronal and sagittal planes. This is evident in the spread of angles for the axial plane, ranging from approximately 30^o to 175^o, than that of both the coronal and sagittal planes, which were predominantly around 90^o.

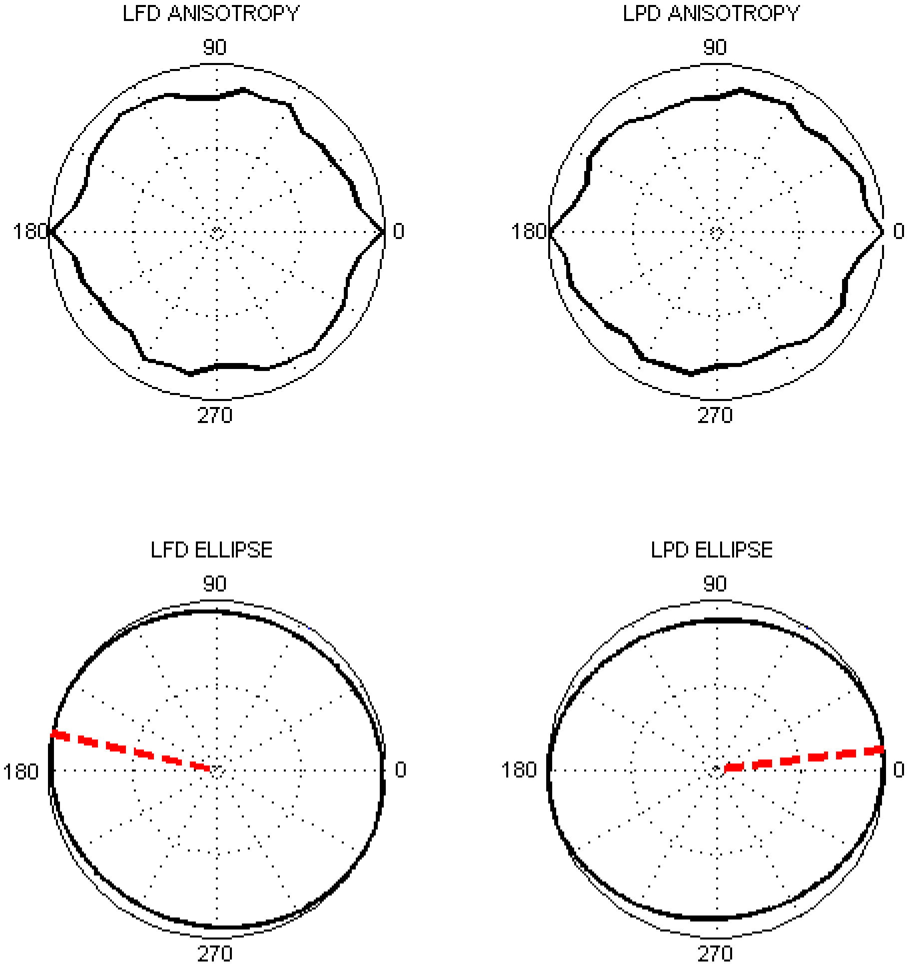

Figure 6.7 Examples of anisotropy measured by the LFD and LPD from the same structure. While the anisotropy data from the LFD and LPD look similar (top), the resulting ellipses have quite different orientations (bottom). Principal orientation is shown by the broken red lines. Data are normalised with respect to the maximum for illustration purposes.

6.3 LPD Anisotropy from Grey and Binary Tomographs

6.3.1 Introduction

In the preceding sections the LPD was introduced and extensive comparisons between the LFD (Chapter 3) and the LPD were made. In the following section the properties of the LPD are explored further.

As a textural measure of anisotropy, LPD can measure anisotropy from the projection of binary tomographs (Section 6.2). However, the LPD can also measure textural anisotropy from the projection of greyscale tomographs. The aim of this section was to explore the ability of the LPD to assess structural anisotropy from greyscale tomographs.

6.3.2 Materials & Methods

The tomographs used in the study described in Section 5.2 (Chapter 5) and Section 6.2 (Chapter 6) were used in this section.

The LPD was measured from the projection of 2D greyscale and binary axial, coronal and sagittal tomographs (Figure 6.4).

The DA was computed using the anisotropy information from the LPD for greyscale (DA_{GRY}) and binary (DA_{BIN}) datasets. The major orientation of the best-fitting ellipse to the LPD anisotropy data of the greyscale (O_{GRY}) and binary (O_{BIN}) datasets were also computed. Comparisons between greyscale LPD and binary LFD (Section 6.2) were also made.

The same statistical techniques applied in Section 6.2 were used in this study.

6.3.3 Results

Degree of Anisotropy

There was no significant difference between DA_{GRY} and DA_{BIN} as measured by the LPD for axial, coronal and sagittal planes (Table 6.5).

Table 6.5 Mean ± standard deviation of DA as computed by the LPD on binary (BINARY) and greyscale (GREY) tomographs. P value indicates significance. DA is dimensionless.

	BINARY (-)	GREY (-)	P
AXIAL	1.21 ± 0.12	1.21 ± 0.13	0.94
CORONAL	1.76 ± 0.31	1.75 ± 0.34	0.20
SAGITTAL	1.51 ± 0.23	1.50 ± 0.23	0.23

Pair-wise analyses indicated an offset (bias) between DA_{BIN} and DA_{GRY} of less than 1.4% (Table 6.6).

Table 6.6 Pair-wise analyses between DA_{BIN} and DA_{GRY} as measured by the LPD. The % column is the ratio ($BIAS/DA_{BIN}$) x 100, which represents the portion of DA_{BIN} that the BIAS represents. Bias and random error are dimensionless

	BIAS (-)	%	RANDOM ERROR (-)
AXIAL	0.00	0.08	0.08
CORONAL	0.02	1.30	0.10
SAGITTAL	0.01	0.85	0.06

The linear relationship between DA_{BIN} and DA_{GRY} was computed for the axial, coronal and sagittal planes (Figure 6.8). Significant ($p < 0.001$) and strong ($r^2 \in [0.67, 0.93]$) relationships were found for all analyses. No significant differences ($p > 0.05$) were found between the slopes or intercepts of regression lines describing the relationship between DA_{BIN} and DA_{GRY} for axial, coronal or sagittal analyses.

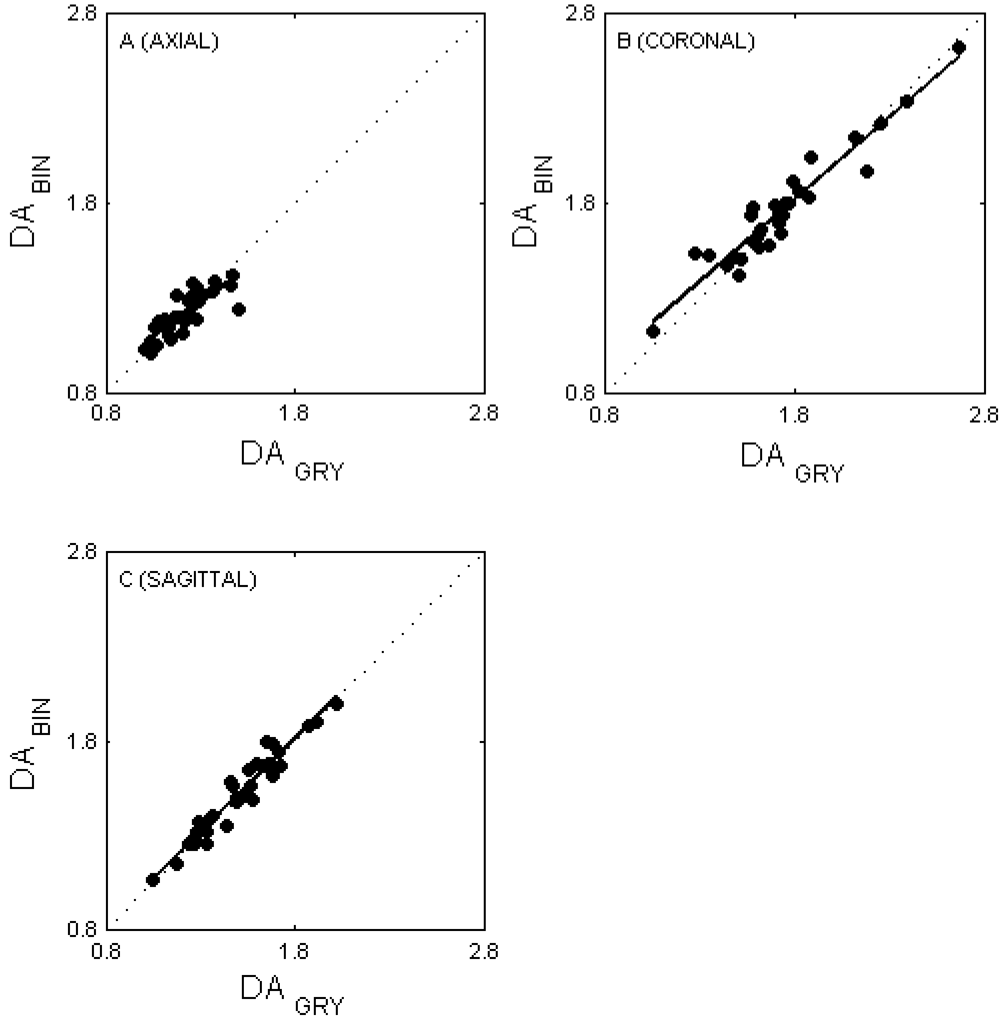

Figure 6.8 Relationship between DA_{BIN} and DA_{GRY} as measured by LPD. [A] Axial: $DA_{BIN} = 0.73(DA_{GRY}) + 0.33$ (n = 32, $r^2 = 0.67$, $p < 0.001$), [B] Coronal: $DA_{BIN} = 0.86(DA_{GRY}) + 0.26$ (n = 32, $r^2 = 0.92$, $p < 0.001$) and [C] Sagittal: $DA_{BIN} = 1.00(DA_{GRY}) + 0.02$ (n = 32, $r^2 = 0.93$, $p < 0.001$).

Principal Orientation

Two data points in the sagittal analyses were identified as being influential outliers and excluded using Cook's distance (Figure 6.9). No significant differences were identified between O_{BIN} and O_{GRY} as measured by LPD for axial (n = 32), coronal (n = 32) or sagittal (n = 30) analyses (Table 6.7).

Table 6.7 Mean ± standard deviation of orientation as computed by the LPD on binary (BINARY) and greyscale (GREY) tomographs. P value indicates significance. Orientation has units of degrees.

	BINARY (DEG.)	GREY (DEG.)	P
AXIAL	93.3 ± 37.2	99.0 ± 38.9	0.17
CORONAL	92.3 ± 15.0	92.3 ± 15.3	0.86
SAGITTAL	85.3 ± 12.5	85.9 ± 12.5	0.44

Pair-wise analyses indicated an offset (bias) between O_{BIN} and O_{GRY} of less than 2% for coronal and sagittal planes and less than 6.5% for the axial plane (Table 6.8).

Table 6.8 Pair-wise analyses between O_{BIN} and O_{GRY} as measured by the LPD. The % column is the ratio ($BIAS/O_{BIN}$) x 100, which represents the portion of O_{BIN} that the BIAS represents. Bias and random error have units of degrees.

	BIAS (DEG.)	%	RANDOM ERROR (DEG.)
AXIAL	5.69	6.10	22.80
CORONAL	0.06	0.07	2.10
SAGITTAL	0.60	1.03	4.15

The relationship between O_{GRY} and O_{BIN} was computed for the axial, coronal and sagittal planes, respectively (Figure 5.10). Significant ($p < 0.001$) relationships were found for all analyses. No significant differences ($p > 0.05$) were found between the slopes or intercepts of regression lines describing the relationship between O_{GRY} and O_{BIN} for axial, coronal or sagittal analyses.

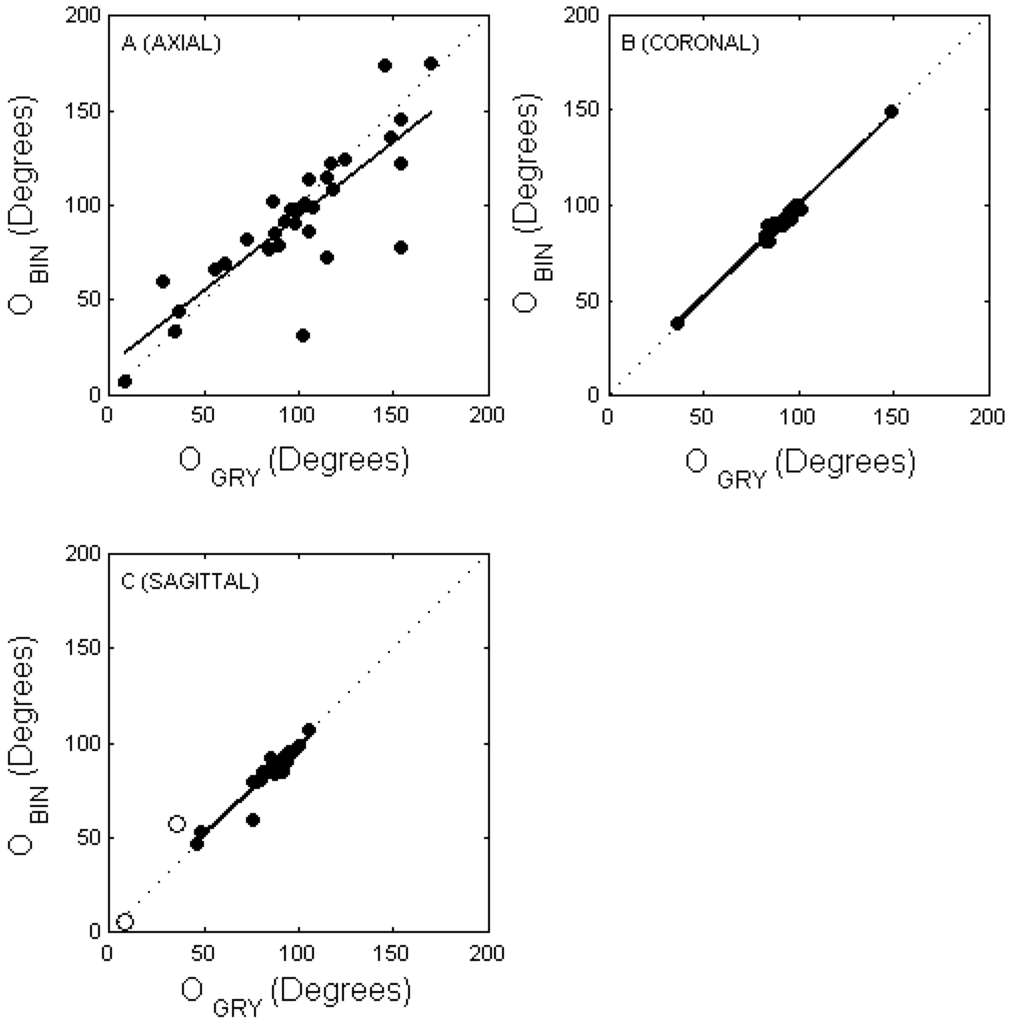

Figure 6.9 Linear relationships between O_{BIN} and O_{GRY}, as measured by LPD. [A] Axial: $O_{BIN} = 0.79(O_{GRY}) + 15.49$ (n = 32, $r^2 = 0.68$, $p < 0.001$), [B] Coronal: $O_{BIN} = 0.98(O_{GRY}) + 2.28$ (n = 32, $r^2 = 0.98$, $p < 0.001$) and [C] Sagittal (excluding 2 outliers; open circles): $O_{BIN} = 0.91(O_{GRY}) + 7.52$ (n = 30, $r^2 = 0.89$, $p < 0.001$).

Binary LFD versus Greyscale LPD

Comparisons between the DA as measured from binary tomographs using the LFD (Section 6.2) and from projections of greyscale tomographs using the LPD (Section 6.3) were made. No significant differences were found between DA as measured from binary tomographs using the LFD and DA measured from the projection of greyscale tomographs using the LPD (Table 6.9).

Table 6.9 Mean ± standard deviation of DA as computed by the LFD on binary (BINARY) and by the LPD from projections of greyscale (GREY) tomographs. P value indicates significance. DA is dimensionless.

	BINARY (-)	GREY (-)	P
AXIAL	1.21 ± 0.12	1.21 ± 0.13	0.99
CORONAL	1.74 ± 0.31	1.75 ± 0.34	0.76
SAGITTAL	1.49 ± 0.25	1.50 ± 0.23	0.49

Pair-wise analyses indicated an offset (bias) between the two measures of less than 1% (Table 6.10).

The linear relationship between DA as computed by each measure was investigated for axial, coronal and sagittal planes (Figure 6.10). Significant and strong relationships were identified for all analyses. No significant differences were identified between the slopes or intercepts of regression lines describing the relationship between the two techniques.

Table 6.10 Pair-wise analyses between DA as measured from binary tomographs by the LFD and DA as measured by the LPD off the projection of greyscale tomographs. The % column is the ratio (BIAS/DA_{LFD}) x 100, which represents the portion of DA_{LFD} that the BIAS represents. Bias and random error are dimensionless

	BIAS (-)	%	RANDOM ERROR (-)
AXIAL	0.00	0.01	0.11
CORONAL	0.01	0.54	0.17
SAGITTAL	0.01	0.90	0.11

Comparisons between orientation as measured from binary images using the LFD (Section 6.2) and from projections of greyscale tomographs using the LPD (Section 6.3) for axial, coronal and sagittal planes were also made. No significant differences were found between orientation as measured off binary tomographs using the LFD and those measured from the projection of greyscale tomographs using the LPD (Table 6.10).

Pair-wise analyses indicated an offset (bias) between the two measures of less than 2% for coronal and sagittal planes and less than 11% for the axial plane (Table 6.12).

The relationship between orientation as computed by each measure was investigated for axial, coronal and sagittal planes (Figure 6.11). Significant and strong relationships were identified for all analyses. Similar to DA, no significant differences were identified between the slopes or intercepts of regression lines describing the relationship between the two techniques.

Table 6.11 Mean ± standard deviation of orientation as computed by the LFD on binary (BINARY) and by the LPD on projections of greyscale (GREY) tomographs. P value indicates significance. Orientation has units of degrees.

	BINARY (DEG.)	GREY (DEG.)	P
AXIAL	92.2 ± 32.7	101.9 ± 35.8	0.12
CORONAL	91.3 ± 6.4	92.3 ± 5.4	0.17
SAGITTAL	87.7 ± 9.9	84.3 ± 15.3	0.81

Table 6.12 Pair-wise analyses between DA as measured from binary tomographs by the LFD and DA as measured by the LPD off the projection of greyscale tomographs. The % column is the ratio ($BIAS/DA_{LFD}$) x 100, which represents the portion of DA_{LFD} that the BIAS represents. Bias and random error are dimensionless.

	BIAS (-)	%	RANDOM ERROR (-)
AXIAL	0.00	0.08	0.08
CORONAL	0.02	1.30	0.10
SAGITTAL	0.01	0.85	0.06

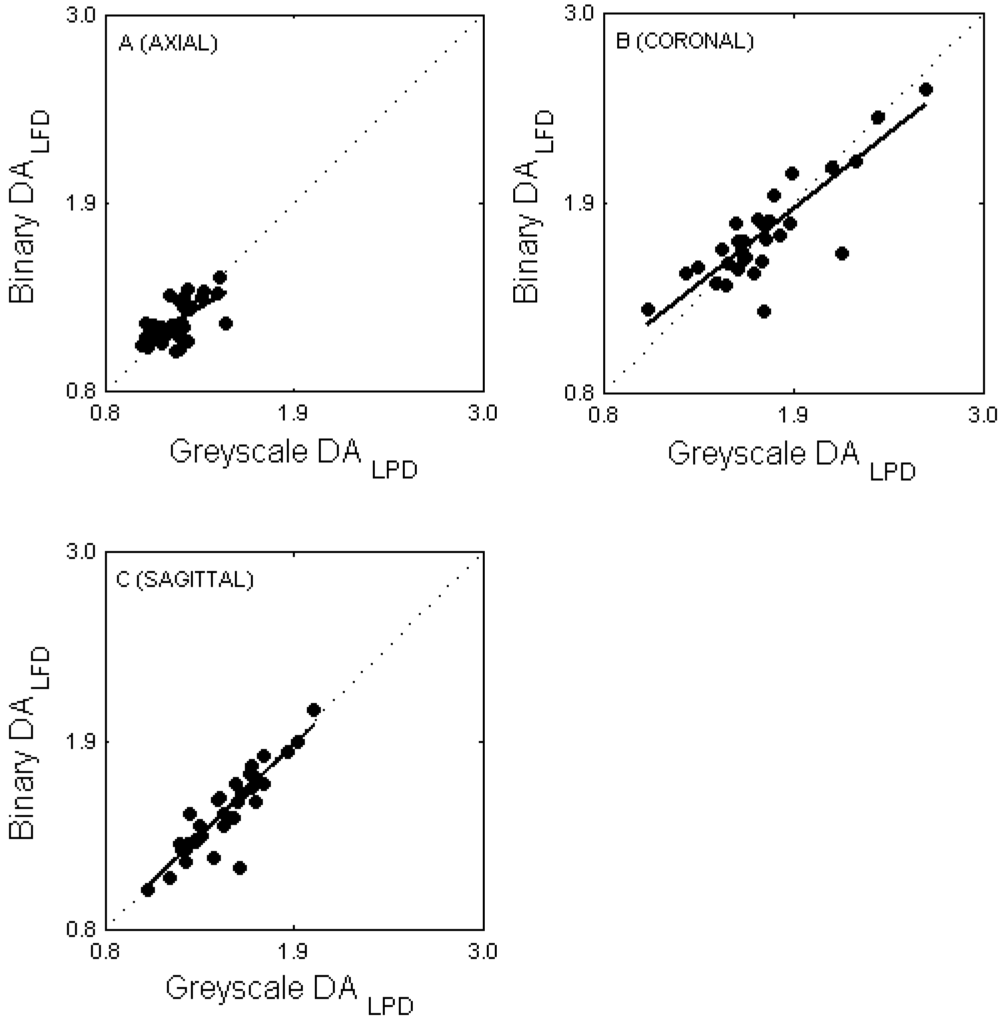

Figure 6.10 Linear relationships between DA measured by LFD on binary tomographs and LPD on projections of greyscale tomographs. [A] Axial: $DA_{LFD} = 0.58(DA_{LPD}) + 0.51$ (n = 32, $r^2 = 0.41$, $p < 0.001$), [B] Coronal: $DA_{LFD} = 0.79(DA_{LPD}) + 0.36$ (n = 32, $r^2 = 0.74$, $p < 0.001$) and [C] Sagittal: $DA_{LFD} = 0.98(DA_{LPD}) + 0.02$ (n = 32, $r^2 = 0.80$, $p < 0.001$).

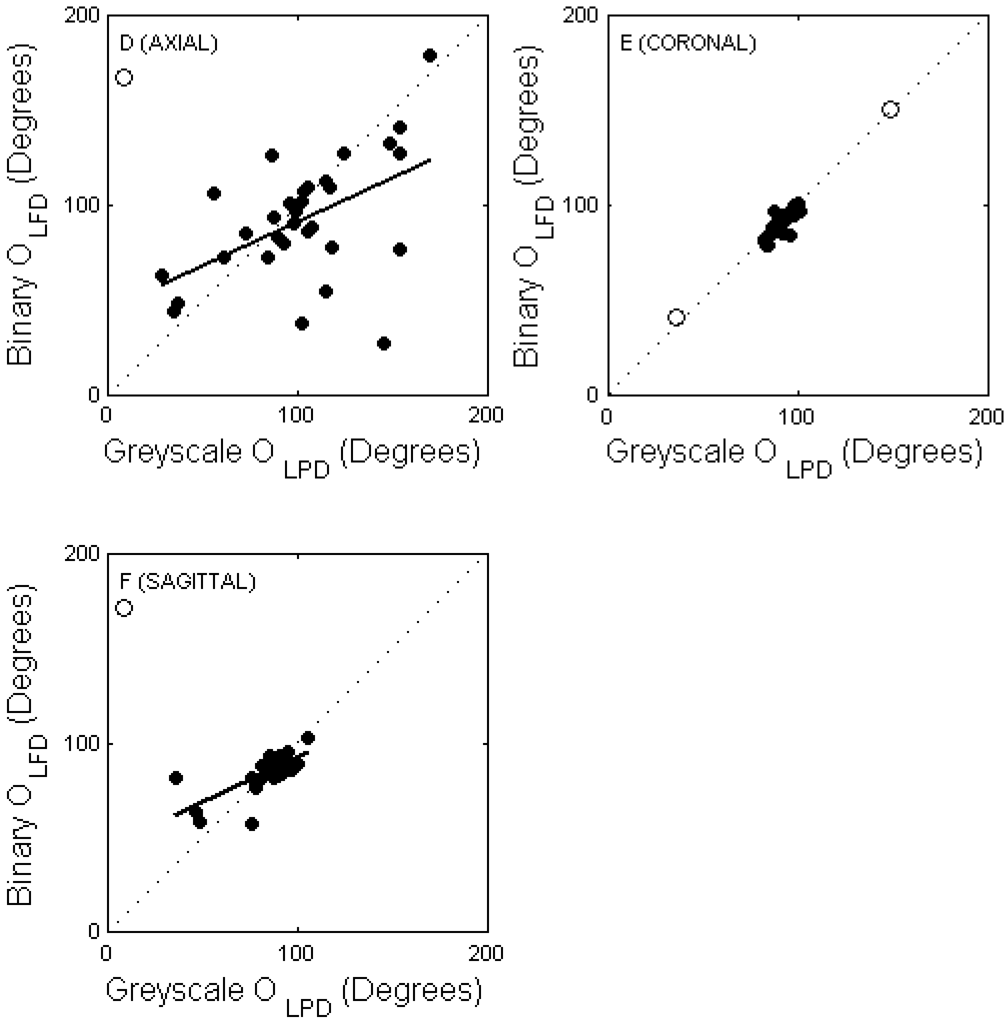

Figure 6.11 Linear relationships between orientation measured by LFD on binary tomographs and LPD on projections of greyscale tomographs. [A] Axial (excluding 1 outlier; open circle): $O_{LFD} = 0.46(O_{LPD}) + 44.97$ (n = 32, r^2 = 0.26, p < 0.001), [B] Coronal (excluding 2 outliers; open circles): (n = 30, $O_{LFD} = 0.98(O_{LPD}) + 1.23$, r^2 = 0.68, p < 0.001) and [D] Sagittal (excluding 1 outlier; open circle): $O_{LFD} = 0.46(O_{LPD}) + 46.41$ (n = 31, r^2 = 0.91, p < 0.001).

6.3.4 Discussion

The LPD was capable of extracting the same architectural information from projections of unsegmented greyscale tomographs as from projections of segmented binary tomographs. No significant differences were identified between DA or orientation using greyscale or binary projections. Regression analyses also showed strong linear relationships between variables measured from greyscale projections and those measured from binary projections. These results show that the LPD can be measured from projections of unsegmented images.

In addition, the LPD was capable of extracting the same architectural information from projections of greyscale tomographs as the LFD extracted from binary tomographs. While, the relationships were not as strong as those seen between greyscale and binary LPD comparisons, the relationships between greyscale LPD and binary LFD show that the LPD can capture detailed structural information from the projections just as effectively as the LFD can from the tomographs. Discrepancies between techniques are most likely due to the fact that the process of segmentation introduces some structural differences (Figure 6.11).

Outliers were identified in the orientation analyses. One axial, two coronal and one sagittal data point were identified as outliers that exerted influence on the regression line. These outliers were identified and excluded from analyses based on Cook’s distance, which is commonly used in statistical analyses (1). While the axial and sagittal outliers where likely to be due to slight ellipse fitting discrepancies (Figure 6.7), the coronal outliers where excluded based on their influence over the regression line and not due to orientation differences.

In this chapter the LPD was introduced and some of its properties explored. The LPD was as effective as the LFD in extracting architectural information from trabecular bone structures. In addition, LPD based architectural properties measured from unsegmented greyscale tomographs were shown to be equal to that measured from segmented binary images. These findings illustrate the ability of the LPD to assess structural anisotropy.

In the next chapter the ability of structural anisotropy, as measured by LPD, in evaluating mechanical competence of trabecular bone samples is explored.

References

1. Field, A. Discovering Statistics Using SPSS: Sage; 2005.
2. Geraets, W. G. Comparison of two methods for measuring orientation. Bone 23:383-8; 1998.
3. Geraets, W. G., Van der Stelt, P. F., Lips, P., Elders, P. J., Van Ginkel, F. C., and Burger, E. H. Orientation of the trabecular pattern of the distal radius around the menopause. J Biomech 30:363-70; 1997.
4. Russ, J. C. Image Processing Handbook: CRC Press; 2002.
5. Whitehouse, W. J. The quantitative morphology of anisotropic trabecular bone. J Microsc 101 Pt 2:153-68; 1974.

Chapter Seven

Explaining Variance in Mechanical Properties with Measures of Structural Anisotropy

7.1 Introduction

In the previous chapters the structural anisotropy of trabecular bone and non-invasive techniques for assessing the anisotropy of trabecular bone were introduced. The PMIL (Chapter 5) is a technique capable of extracting MIL based information from the projection of trabecular bone samples. This technique allows information regarding the total bone surface (BS/TV) to be accessed via projections of the trabecular bone structure. The combination of BS/TV with BV/TV allows one to access parallel-plate model based information of the structures in question (Appendix B). The LPD (Chapter 6) is a technique capable of assessing structural anisotropy from projections of trabecular bone samples. Similar to the LFD (Chapter 3), the structural anisotropy information obtained via the LPD is more sensitive to architectural variations than the MIL (Chapter 3) and PMIL.

Structural anisotropy has in the past been shown to be a significant contributor to the mechanical competence (1-3, 9, 24) and orthotropic elastic properties (5, 6, 10, 15, 26) of trabecular bone. As such, the aim of this chapter was to determine the roles of PMIL and LPD in the mechanical competence of vertebral trabecular bone via statistical modelling. Using data from Chapter 4 the PMIL and LPD were used in multivariate regression models to explain the variance in apparent ultimate failure stress, apparent modulus of elasticity and apparent modulus of toughness, for trabecular bone samples mechanically tested in both first overload and second overload experiments.

7.2 Materials and Methods

The trabecular bone cubes described in Section 4.2 of Chapter 4 were also used in the work reported in this chapter. Briefly, at postmortem examination, the T12/L1 vertebral bodies from 5 cases (4 males and 1 female) and the L4/L5 vertebral bodies from 7 cases (5 males and 2 females) were collected. A cube of trabecular bone 10x10x10 mm was obtained from the centrum of each vertebral body. Cubes from each T12/L1 and L4/L5 pair were assigned to either superoinferior (SI) or anteroposterior (AP) mechanical testing groups using a random selection process (Chapter 4).

Bone mineral content (BMC) of all trabecular bone cubes was determined using dual energy x-ray absorptiometry (DXA) (12, 14) (Chapter 2, Section 2.2.3). Volumetric bone mineral density (vBMD) was then calculated by normalising the BMC by the apparent volume of the cubes as calculated from cube dimensions measured by digital callipers (Chapter 2, Section 2.2.1). Trabecular bone cubes were then imaged using a Skyscan 1072 x-ray microcomputed tomography (μCT) system (Chapter 2, Section 2.2.2). Tomographic images obtained from scanning were binarised and a component-labelling routine used to remove any unconnected components (Chapter 2, Section 2.2.2). Standard model-independent 3D algorithms were employed to calculate the bone volume fraction (BV/TV [%]), total surface ($BS/TV_{\mu CT}$ [mm^2/mm^3]) and degree of anisotropy ($DA_{\mu CT}$) (Chapter 2, Section 2.2.2). These parameters were computed using CTAn software provided by the manufacturer of the μCT system (Skyscan). Axial PMIL based total surface (BS/TV_{PMIL} [mm^2/mm^3]) (Chapter 5) and sagittal LPD based degree of anisotropy (DA_{LPD}) (Chapter 6) were also measured from each dataset using custom written applications (Matlab, The Mathworks).

Mechanical testing was carried out as described in Section 4.2 of Chapter 4 (Figure 7.1). The apparent ultimate failure stress (UFS), apparent modulus of elasticity (E) and apparent modulus of toughness (*u*) (Chapter 2, Section 2.2.4) were computed from the first and second overload tests of the SI and AP groups (Section 4.2, Chapter 4).

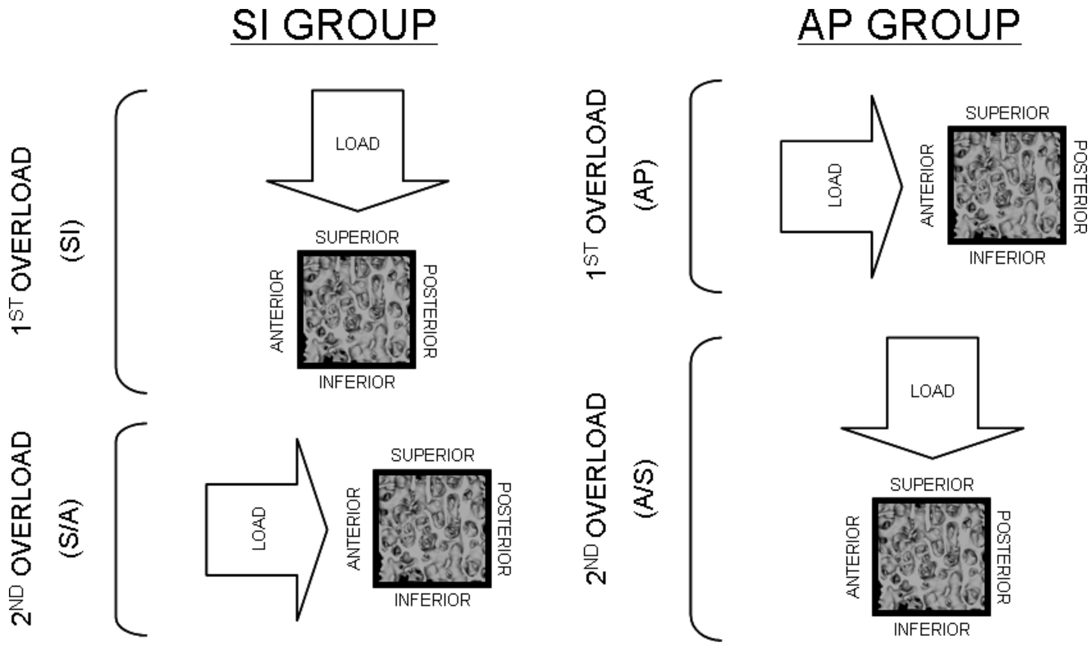

Figure 7.1 Schematic diagram of mechanical testing protocol.

Linear univariate regression analyses were used to test relationships between variables. Linear multivariate regression analyses were used to test different models in their ability to explain the variance in mechanical parameters. To quantify the ability of multivariate models to account for the variance in mechanical properties, r^2 was determined. Model coefficients were tested against being significantly different from zero using the t-statistic. All statistical analyses were performed using a combination of standard routines within SPSS (SPSS Inc.) and Matlab (The Mathworks).

7.3 Results

7.3.1 Bone Architecture

Bone architecture results are described in Section 4.3.1 of Chapter 4. Briefly, there was no significant difference in BV/TV or microarchitecture between males and females or between trabecular bone cubes assigned to SI or those assigned to AP.

7.3.2 Univariate Analyses for First Overloads

Significant ($p < 0.05$) relationships were found between mechanical parameters. As expected (7, 11, 12) there were significant and strong relationships between UFS and E in both SI and AP mechanical tests (Table 7.1 and 7.2, respectively) (Figures 7.2).

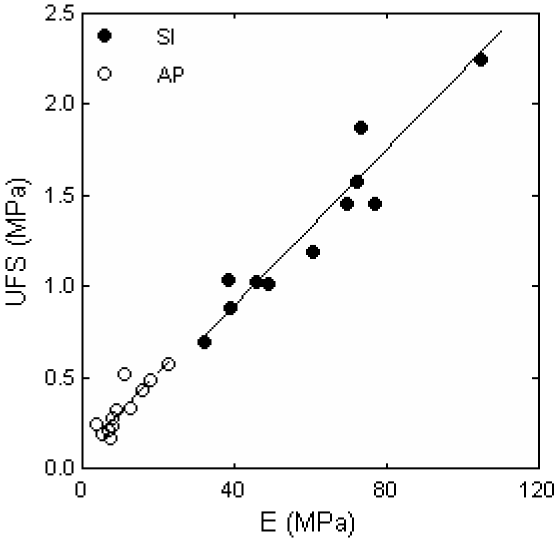

Figure 7.2 Relationship between UFS and E for the SI and AP mechanical tests. SI: UFS = 0.02E + 0.03, n = 12, r^2 = 0.95 and $p < 0.001$) and AP: UFS = 0.02E + 0.11 (n = 12, r^2 = 0.70 and $p < 0.001$). Regression line for SI data is shown as a solid line and regression line for AP data is shown as a broken line.

Significant relationships were found between *u* and both UFS and E in the SI mechanical tests (Table 7.1), however no such relationship was found in the AP mechanical tests (Table 7.2).

In SI mechanical tests, UFS was only significantly correlated to BV/TV, while in the AP tests UFS was significantly correlated to both BV/TV and vBMD. A significant relationship was found between *u* and BV/TV for SI mechanical tests. No such relationship was found in AP mechanical tests. Similarly, no significant relationships were found between *u* and vBMD.

Power-law relationships between E and BV/TV (23, 25) for SI mechanical tests ($E_{SI} = 0.16\left(\frac{BV}{TV}_{SI}\right)^{2.5}$, n = 12, $r^2 = 0.72$ and $p < 0.05$) produced only marginal improvements over the linear relationship (Table 7.2), while for AP mechanical tests the power-law relationship ($E_{AP} = 0.01\left(\frac{BV}{TV}_{AP}\right)^{2.9}$, n = 12, $r^2 = 0.51$ and $p < 0.05$) was marginally worse than the linear relationship (Table 7.2). No significant relationship was found between E and vBMD.

Significant relationships were found between total surface as measured by µCT ($BS/TV_{\mu CT}$) and PMIL (BS/TV_{PMIL}) for both SI (Table 7.1) and AP (Table 7.2) groups. A significant relationship was also found between degree of anisotropy as measured by µCT ($DA_{\mu CT}$) and by LPD (DA_{LPD}) for the AP group (Table 7.2) but not for the SI group (Table 7.1).

Differences between SI and AP mechanical tests were also reflected in the relationship between architectural and mechanical parameters. In the SI mechanical tests the only significant relationship was between *u* and $BS/TV_{\mu CT}$ (Table 7.1). However, in the AP mechanical tests both UFS and E showed significant relationships to both $BS/TV_{\mu CT}$ and BS/TV_{PMIL} (Table 7.2). No significant univariate relationships were found between mechanical parameters and degree of anisotropy.

Table 7.1 Linear univariate regression relationships between superoinferior (SI) mechanical and architectural parameters showing Pearson's correlation coefficient (r) and significance. Shaded boxes highlight significant ($p < 0.05$) relationships.

r	UFS_{SI}	E_{SI}	u_{SI}	BV/TV	vBMD	$BS/TV_{\mu CT}$	BS/TV_{PMIL}	$DA_{\mu CT}$	DA_{LPD}
UFS_{SI}	-								
E_{SI}	0.97 $p < 0.001$	-							
u_{SI}	0.98 $p < 0.001$	0.93 $p < 0.001$	-						
BV/TV	0.88 $p < 0.001$	0.83 $p < 0.002$	0.89 $p < 0.001$	-					
vBMD	0.43 $p = 0.16$	0.39 $p = 0.22$	0.42 $p = 0.18$	0.65 $p = 0.02$	-				
$BS/TV_{\mu CT}$	0.56 $p = 0.06$	0.44 $p = 0.16$	0.64 $p = 0.02$	0.73 $p < 0.01$	0.59 $p = 0.04$	-			
BS/TV_{PMIL}	0.37 $p = 0.24$	0.27 $p = 0.40$	0.47 $p = 0.12$	0.58 $p < 0.05$	0.46 $p = 0.13$	0.74 $p < 0.01$	-		
$DA_{\mu CT}$	-0.10 $p = 0.76$	-0.09 $p = 0.77$	-0.10 $p = 0.76$	0.06 $p = 0.86$	0.48 $p = 0.11$	0.08 $p = 0.82$	0.20 $p = 0.53$	-	
DA_{LPD}	-0.25 $p = 0.43$	-0.28 $p = 0.38$	-0.23 $p = 0.47$	-0.15 $p = 0.64$	0.12 $p = 0.70$	0.00 $p = 0.99$	0.35 $p = 0.26$	0.18 $p = 0.57$	-

Table 7.2 Linear univariate regression relationships between anteroposterior (AP) mechanical and architectural parameters showing Pearson's correlation coefficient (r) and significance. Shaded boxes highlight significant ($p < 0.05$) relationships.

r	UFS_{AP}	E_{AP}	u_{AP}	BV/TV	vBMD	$BS/TV_{\mu CT}$	BS/TV_{PMIL}	$DA_{\mu CT}$	DA_{LPD}
UFS_{AP}	-								
E_{AP}	0.87 $p < 0.001$	-							
u_{AP}	0.57 $p = 0.05$	0.18 $p = 0.58$	-						
BV/TV	0.78 $p < 0.01$	0.73 $p < 0.01$	0.12 $p = 0.72$	-					
vBMD	0.68 $p = 0.01$	0.55 $p = 0.07$	0.23 $p = 0.46$	0.79 $p < 0.01$	-				
$BS/TV_{\mu CT}$	0.80 $p < 0.01$	0.77 $p < 0.01$	0.26 $p = 0.41$	0.78 $p < 0.001$	0.50 $p = 0.10$	-			
BS/TV_{PMIL}	0.88 $p < 0.001$	0.82 $p < 0.001$	0.35 $p = 0.27$	0.84 $p < 0.001$	0.66 $p = 0.02$	0.91 $p < 0.001$	-		
$DA_{\mu CT}$	-0.46 $p = 0.13$	-0.53 $p = 0.07$	-0.43 $p = 0.16$	0.05 $p = 0.87$	0.05 $p = 0.87$	-0.37 $p = 0.23$	-0.40 $p = 0.20$	-	
DA_{LPD}	-0.45 $p = 0.14$	-0.54 $p = 0.07$	-0.30 $p = 0.34$	-0.01 $p = 0.97$	0.02 $p = 0.94$	-0.44 $p = 0.15$	-0.35 $p = 0.26$	0.88 $p < 0.001$	-

7.3.3 Multivariate Analyses for First Overloads

Similar to univariate analyses, differences were observed between SI and AP mechanical tests. In the SI group, no significant contribution was made by any parameter in explaining the variance in mechanical properties beyond that explained by BV/TV alone (Figure 7.3). In contrast, in the AP group, significant improvements were found with the addition of structural parameters to BV/TV or vBMD alone.

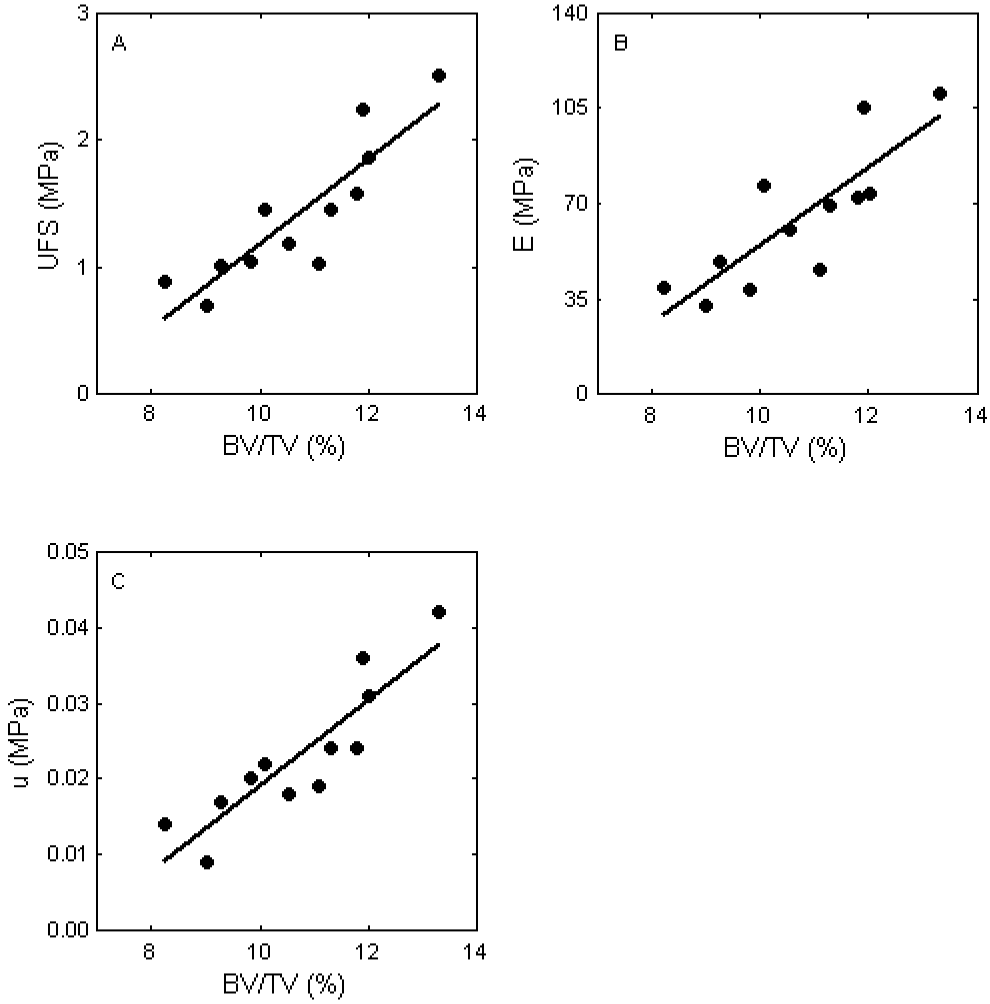

Figure 7.3 Relationship between BV/TV and the mechanical parameters UFS, E and u. [A] UFS = 0.33(BV/TV) – 2.16 (n = 12, $r^2 = 0.77$ and $p < 0.001$), [B] E = 14.32(BV/TV) – 88.87 (n = 12, $r^2 = 0.69$ and $p < 0.001$) and [C] u = 0.006(BV/TV) – 0.04 (n = 12, $r^2 = 0.79$ and $p < 0.001$).

For µCT parameter based analyses, the addition of $DA_{\mu CT}$ to BV/TV significantly improved the amount of variance explained by 25%, from 61% to 86% for UFS_{AP}, and by 33%, from 53% to 86% for E_{AP} over BV/TV alone (Figure 7.4 & Table 7.3). $BS/TV_{\mu CT}$ or the linear combination of $BS/TV_{\mu CT}$ and $DA_{\mu CT}$ with BV/TV did not produce any significant improvements in the amount of variance explained in AP mechanical properties over BV/TV alone.

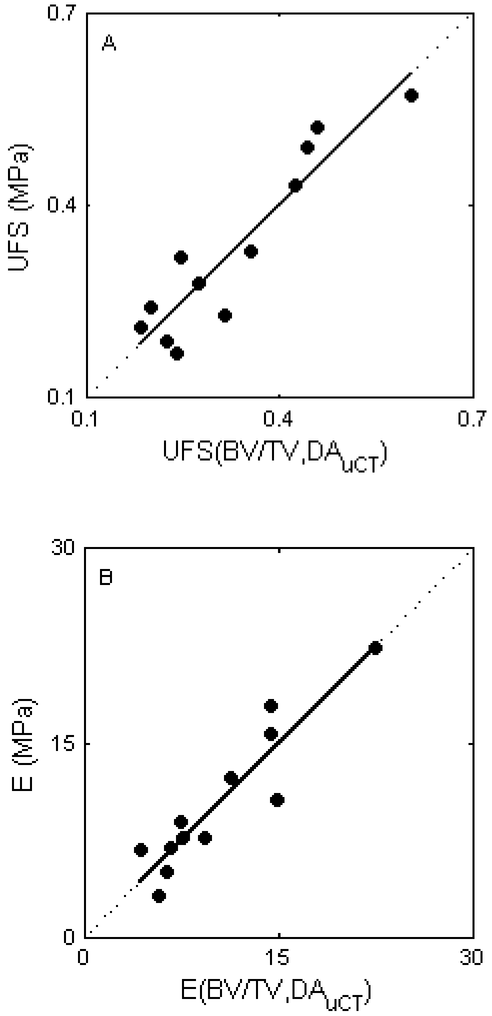

Figure 7.4 Relationships between µCT parameter (BV/TV and $DA_{\mu CT}$) based models for AP UFS and AP E. [A] UFS(BV/TV, $DA_{\mu CT}$) = 0.08(BV/TV) – 0.26($DA_{\mu CT}$)+ 0.06 (n = 12, $r^2 = 0.86$, $p < 0.01$); [B] E(BV/TV, $DA_{\mu CT}$) = 3.02(BV/TV) -12.13($DA_{\mu CT}$) + 4.93 (n = 12, $r^2 = 0.86$ and $p < 0.01$). Dotted lines represent lines of identity.

For DXA and projection based analyses (PMIL and LPD), the addition of DA_{LPD} to vBMD was able to improve the amount of variance explained in UFS_{AP} by 22%, from 47% to 69%, and in E_{AP} by 30%, from 30% to 60%, over vBMD alone (Figure 7.5 & Table 7.3). Although the addition of BS/TV_{PMIL} to vBMD produced a significant increase in the amount of variance explained in UFS_{AP}, the vBMD coefficient of the model was not found to be significantly different from zero ($p = 0.40$). Thus, the higher explanatory value can be attributed predominantly to BS/TV_{PMIL} alone. BS/TV_{PMIL} explained approximately 79% of the variance in UFS_{AP} (Figure 7.6). There was no significant improvement in combining both BS/TV_{PMIL} and DA_{LPD} with vBMD (Table 7.3).

Using BV/TV in combination with the projection based parameters (PMIL and LPD), the addition of DA_{LPD} to BV/TV increased the amount of variance explained in UFS_{AP} by 20%, from 61% to 81%, and in E_{AP} by 28%, from 53% to 81% (Figure 7.7 & Table 7.3). Although the addition of BS/TV_{PMIL} to BV/TV produced a significant increase in the amount of variance explained in UFS_{AP}, the BV/TV coefficient of the model was not found to be significantly different from zero ($p = 0.59$). Thus, the higher explanatory value can be attributed predominantly to BS/TV_{PMIL} alone. BS/TV_{PMIL} explained approximately 79% of the variance in UFS_{AP} (Figure 7.6). The linear combination of BV/TV, BS/TV_{PMIL} and DA_{LPD} did not significantly improve the explanation of the variance in any mechanical parameter.

With the exception of BV/TV in the SI tests, no other parameter or model was able to significantly explain the variance in u.

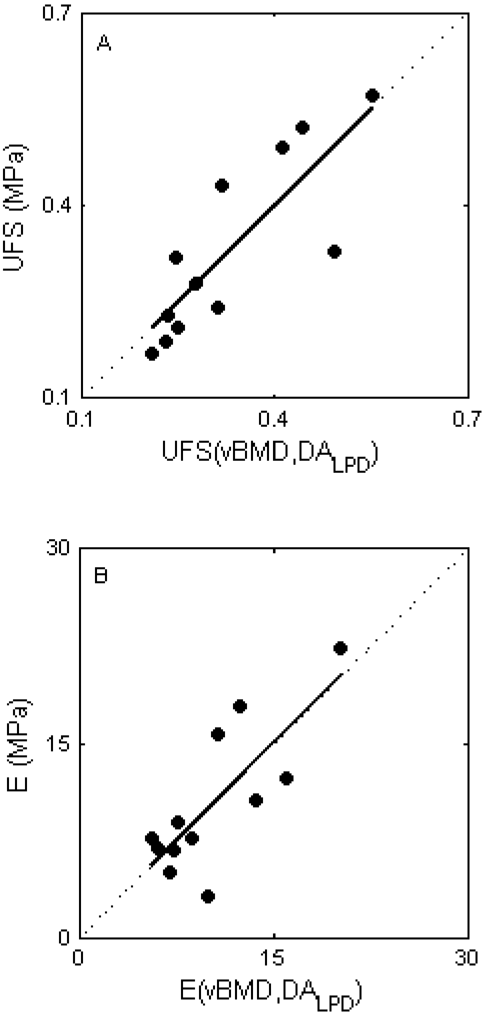

Figure 7.5 Relationship between DXA (vBMD) and LPD based DA (DA_{LPD}) with AP UFS and AP E. [A] UFS(vBMD,DA_{LPD}) = 6.16(vBMD) – 0.47(DA_{LPD}) + 0.59 (n = 12, $r^2 = 0.69$ and $p < 0.01$); [B] E(vBMD,DA_{LPD}) = 205.53(vBMD) – 22.52(DA_{LPD}) + 30.55 (n = 12, $r^2 = 0.60$, $p < 0.01$). Dotted lines represent lines of identity.

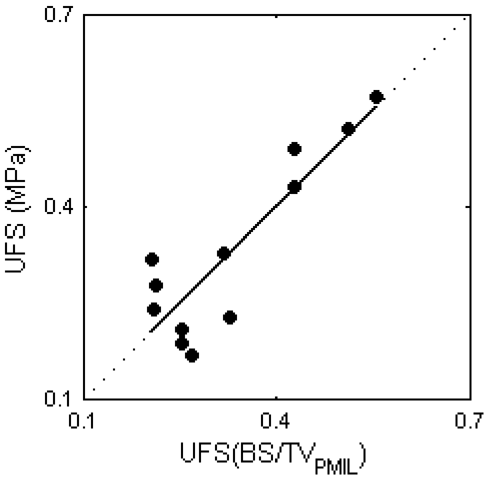

Figure 7.6 Relationship between AP UFS and a univariate model using BS/TV$_{PMIL}$. UFS = 0.69(BS/TV$_{PMIL}$) – 0.75 (n = 12, r^2 = 0.79 and p < 0.001). Dotted line represents line of identity.

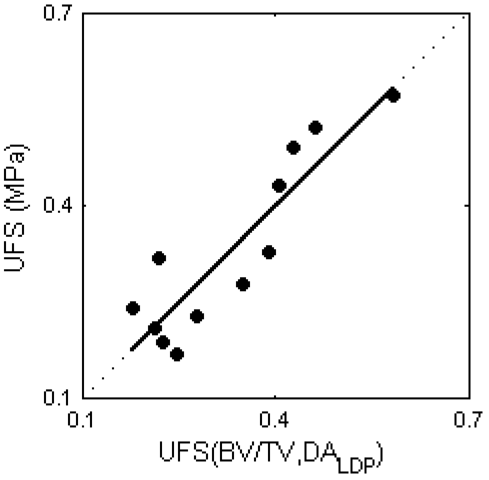

Figure 7.7 Relationship between uCT based BV/TV and projection based DA (DA$_{LPD}$) with AP UFS. UFS(BV/TV,DA$_{LPD}$) = 0.08(BV/TV) – 0.442(DA$_{LPD}$) + 0.267 (n = 12, r^2 = 0.81, p < 0.01). Dotted lines represent lines of identity.

Table 7.3 Coefficient of determination (r^2) and significance of linear multivariate regression analyses between structural and mechanical parameters for superoinferior (SI) and anteroposterior (AP) mechanical testing. P-value indicates significance of the F-statistic change with the addition of a parameter to the model. * indicates that the vBMD coefficient in the model is not significantly different to 0. ** indicates that the BV/TV coefficient in the model is not significantly different to 0.

	Model	**UFS**		**E**		***u***	
		r^2	**p**	**r^2**	**p**	**r^2**	**p**
SI	BV/TV	0.77	< 0.001	0.69	< 0.01	0.79	< 0.001
	BV/TV & BS/TV$_{\mu CT}$	0.79	0.44	0.76	0.16	0.79	0.96
	BV/TV & DA$_{\mu CT}$	0.80	0.34	0.71	0.44	0.81	0.32
	BV/TV, BS/TV$_{\mu CT}$ & DA$_{\mu CT}$	0.81	0.38	0.77	0.46	0.81	0.35
	vBMD	0.19	0.16	0.15	0.22	0.17	0.18
	vBMD & BS/TV$_{PMIL}$	0.22	0.54	0.16	0.74	0.28	0.29
	vBMD & DA$_{LPD}$	0.28	0.31	0.26	0.28	0.26	0.18
	vBMD, BS/TV$_{PMIL}$ & DA$_{LPD}$	0.38	0.20	0.31	0.22	0.45	0.15
	BV/TV & BS/TV$_{PMIL}$	0.80	0.27	0.76	0.15	0.79	0.75
	BV/TV & DA$_{LPD}$	0.79	0.47	0.72	0.40	0.80	0.53
	BV/TV, BV/TV$_{PMIL}$ & DA$_{LPD}$	0.80	0.87	0.76	0.93	0.80	0.62
AP	BV/TV	0.61	< 0.01	0.53	< 0.01	0.01	0.72
	BV/TV & BS/TV$_{\mu CT}$	0.70	0.13	0.63	0.15	0.01	0.40
	BV/TV & DA$_{\mu CT}$	0.86	< 0.01	0.86	< 0.01	0.21	0.17
	BV/TV, BS/TV$_{\mu CT}$ & DA$_{\mu CT}$	0.86	0.13	0.86	0.15	0.21	0.31
	vBMD	0.47	< 0.02	0.30	0.07	0.06	0.46
	vBMD & BS/TV$_{PMIL}$	0.79	< 0.01 *	0.68	0.07	0.12	0.43
	vBMD & DA$_{LPD}$	0.69	0.03	0.60	0.03	0.15	0.34
	vBMD, BS/TV$_{PMIL}$ & DA$_{LPD}$	0.84	0.16	0.76	0.14	0.17	0.54
	BV/TV & BS/TV$_{PMIL}$	0.79	0.03 **	0.68	0.07	0.23	0.15
	BV/TV & DA$_{LPD}$	0.81	< 0.02	0.81	< 0.01	0.10	0.37
	BV/TV, BV/TV$_{PMIL}$ & DA$_{LPD}$	0.84	0.13	0.81	0.07	0.23	0.96

7.3.4 Univariate Analyses for Second Overloads

Significant ($p < 0.05$) relationships were identified between second overload mechanical parameters. As expected (7, 11, 12) there were significant linear relationships between UFS and E in both A/S and S/A mechanical testing groups (Figure 7.8).

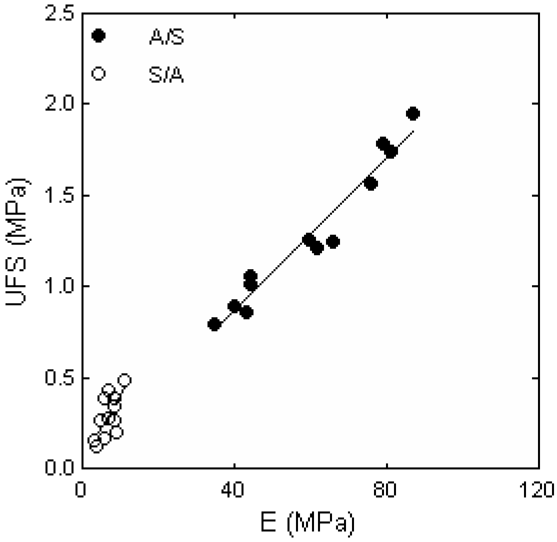

Figure 7.8 Linear relationships between UFS and E for the second overload mechanical tests. A/S denotes superoinferior overload following prior anteroposterior overload and S/A anteroposterior overload following superoinferior overload. A/S: UFS = 0.02E + 0.03 (n = 12, r2 = 0.92 and p < 0.001) and S/A UFS = 0.03E + 0.07 (n = 12, r2 = 0.49 and p = 0.01). Regression line for A/S data is shown as a solid lone and regression line for S/A data is shown as a broken line.

Significant relationships were found between both *u* and E and UFS in the A/S and S/A mechanical tests (Tables 7.4 and 7.5).

Table 7.4 Linear univariate regression relationships between A/S mechanical and AP group architectural parameters, showing Pearson's correlation coefficient (r) and significance. Shaded boxes highlight significant ($p < 0.05$) relationships.

r	UFS$_{A/S}$	E$_{A/S}$	$u_{A/S}$	BV/TV	vBMD	BS/TV$_{\mu CT}$	BS/TV$_{PMIL}$	DA$_{\mu CT}$	DA$_{LPD}$
UFS$_{A/S}$	-								
E$_{A/S}$	0.97 $p < 0.001$	-							
$u_{A/S}$	0.95 $p < 0.001$	0.87 $p < 0.001$	-						
BV/TV	0.62 $p = 0.03$	0.47 $p = 0.12$	0.70 $p = 0.01$	-					
vBMD	0.61 $p = 0.04$	0.51 $p = 0.09$	0.62 $p = 0.03$	0.79 $p < 0.01$	-				
BS/TV$_{\mu CT}$	0.24 $p = 0.45$	0.10 $p = 0.75$	0.37 $p = 0.24$	0.78 $p < 0.01$	0.50 $p = 0.10$	-			
BS/TV$_{PMIL}$	0.32 $p = 0.31$	0.14 0.67	0.49 $p = 0.11$	0.84 $p < 0.01$	0.66 $p = 0.02$	0.91 $p < 0.001$	-		
DA$_{\mu CT}$	0.41 $p = 0.18$	0.51 $p = 0.09$	0.25 $p = 0.44$	0.05 $p = 0.87$	0.05 $p = 0.87$	-0.37 $p = 0.23$	-0.40 $p = 0.20$	-	
DA$_{LPD}$	0.52 $p = 0.08$	0.58 $p < 0.05$	0.40 $p = 0.20$	-0.01 $p = 0.97$	0.02 $p = 0.94$	-0.44 $p = 0.15$	-0.35 $p = 0.26$	0.88 $p < 0.001$	-

Table 7.5 Linear univariate regression relationships between S/A mechanical and SI group architectural parameters, showing Pearson's correlation coefficient (r) and significance. Shaded boxes highlight significant ($p < 0.05$) relationships.

r	$UFS_{S/A}$	$E_{S/A}$	$u_{S/A}$	BV/TV	vBMD	$BS/TV_{\mu CT}$	BS/TV_{PMIL}	$DA_{\mu CT}$	DA_{LPD}
$UFS_{S/A}$	-								
$E_{S/A}$	0.67 $p = 0.02$	-							
$u_{S/A}$	0.79 $p < 0.01$	0.25 $p = 0.44$	-						
BV/TV	0.82 $p < 0.01$	0.45 $p = 0.14$	0.87 $p < 0.001$	-					
vBMD	0.25 $p = 0.44$	0.28 $p = 0.38$	0.40 $p = 0.20$	0.65 $p = 0.02$	-				
$BS/TV_{\mu CT}$	0.50 $p = 0.10$	0.35 $p = 0.26$	0.59 $p < 0.05$	0.73 $p < 0.01$	0.59 $p = 0.04$	-			
BS/TV_{PMIL}	0.34 $p = 0.28$	0.37 $p = 0.24$	0.44 $p = 0.15$	0.58 $p < 0.05$	0.46 $p = 0.13$	0.74 $p < 0.01$	-		
$DA_{\mu CT}$	-0.17 $p = 61$	-0.11 $p = 0.74$	-0.07 $p = 0.83$	0.06 $p = 0.85$	0.48 $p = 0.11$	0.08 $p = 0.81$	0.20 $p = 0.53$	-	
DA_{LPD}	-0.37 $p = 0.24$	-0.07 $p = 0.82$	-0.11 $p = 0.74$	-0.15 $p = 0.64$	0.12 $p = 0.70$	0.00 $p = 0.99$	0.35 $p = 0.26$	0.18 $p = 0.57$	-

Relationships between mechanical and architectural parameters were different to those identified in the first overload tests. UFS was significantly correlated to BV/TV and vBMD in the A/S group and only BV/TV in the S/A group. Significant relationships were also identified between *u* and BV/TV in both groups. No such relationships were observed between E and BV/TV or E and vBMD (Tables 7.4 and 7.5).

Since architectural parameters were only measured prior to the first overload, the relationships between architectural parameters were the same as those reported in the first overload analyses (Section 7.3.2).

Unlike the first overload tests, no significant relationship was identified between total surface as measured by µCT ($BS/TV_{\mu CT}$) or PMIL (BS/TV_{PMIL}) and UFS or E for both A/S (Table 7.4) and S/A (Table 7.5) groups. Significant relationships were observed between $u_{S/A}$ and $BS/TV_{\mu CT}$ (Table 7.5) and $E_{A/S}$ and DA_{LPD} (Table 7.4).

7.3.5 Multivariate Analyses for Second Overloads

Differences were identified between A/S and S/A groups in multivariate analyses. These were different to the relationships identified in the first overload multivariate analyses. In the S/A group, no significant contribution was made by any parameter in explaining the variance in UFS and *u* beyond that explained by BV/TV alone (Figure 7.9 and Table 7.6). By contrast, in the A/S group, significant improvements were found with the addition of structural parameters to BV/TV or vBMD (Table 7.6).

Table 7.6 Coefficient of determination (r^2) and significance of linear multivariate regression analyses between structural and mechanical parameters for the A/S and S/A mechanical testing groups. P-value indicates significance of the F-statistic change with the addition of a parameter to the model.

	Model	**UFS**		**E**		***u***	
		r^2	**p**	**r^2**	**p**	**r^2**	**p**
A/S	BV/TV	0.38	0.03	0.23	0.12	0.46	0.02
	BV/TV & BS/TV$_{\mu CT}$	0.53	0.12	0.41	0.13	0.54	0.23
	BV/TV & DA$_{\mu CT}$	0.53	0.13	0.46	0.08	0.51	0.38
	vBMD	0.37	0.04	0.19	0.09	0.37	0.04
	vBMD & BS/TV$_{PMIL}$	0.38	0.69	0.18	0.35	0.38	0.73
	vBMD & DA$_{LPD}$	0.62	0.04	0.58	0.03	0.53	0.11
	BV/TV & BS/TV$_{PMIL}$	0.51	0.16	0.45	0.09	0.49	0.50
	BV/TV & DA$_{LPD}$	0.66	0.02	0.57	0.03	0.64	0.06
S/A	BV/TV	0.68	0.001	0.20	0.14	0.77	< 0.001
	BV/TV & BS/TV$_{\mu CT}$	0.70	0.43	0.20	0.92	0.78	0.71
	BV/TV & DA$_{\mu CT}$	0.72	0.21	0.22	0.66	0.79	0.46
	vBMD	0.06	0.44	0.08	0.38	0.16	0.19
	vBMD & BS/TV$_{PMIL}$	0.13	0.43	0.15	0.41	0.25	0.34
	vBMD & DA$_{LPD}$	0.23	0.20	0.09	0.74	0.19	0.57
	BV/TV & BS/TV$_{PMIL}$	0.70	0.40	0.22	0.67	0.78	0.62
	BV/TV & DA$_{LPD}$	0.74	0.18	0.20	0.98	0.77	0.96

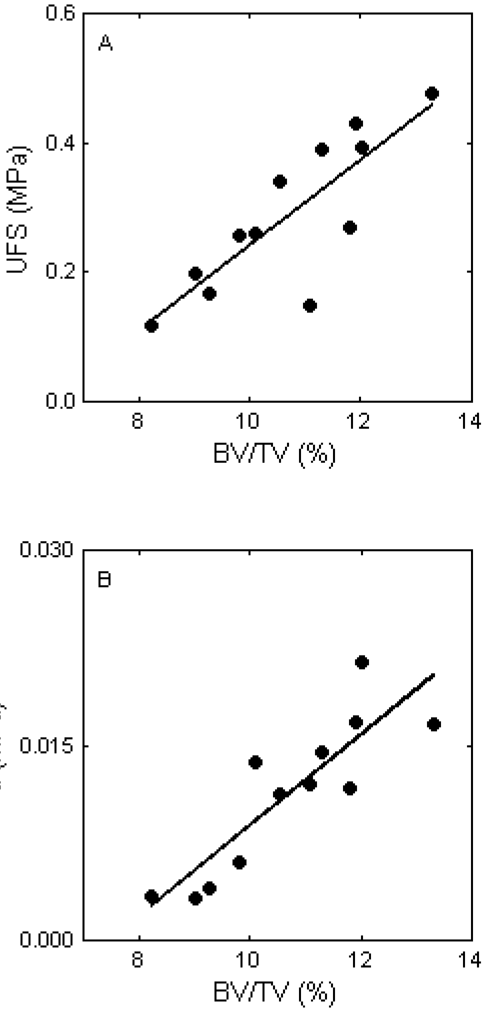

Figure 7.9 Linear relationships between S/A UFS and S/A u and BV/TV. [A] $UFS_{S/A} = 0.07BV/TV_{SI} – 0.42$ (n = 12, $r^2 = 0.68$ and $p < 0.01$) and [B] $u_{S/A} = 0.004BV/TV_{SI} – 0.02$ (n = 12, $r^2 = 0.75$ and $p < 0.01$).

Models that better explain the variance in mechanical parameters were found in the A/S group. The addition of DA_{LPD} to vBMD did significantly improve the amount of variance explained by 25%, from 37% to 62% for $UFS_{A/S}$, and by 39%, from 19% to 58% for $E_{A/S}$ (Table 7.6 and Figure 7.10). Similar results were identified with the addition of DA_{LPD} to BV/TV (Table 7.6 and Figure 7.11). The addition of $BS/TV_{\mu CT}$ and $DA_{\mu CT}$ did not significantly improve the amount of variance explained in any mechanical parameter beyond that explained by BV/TV alone.

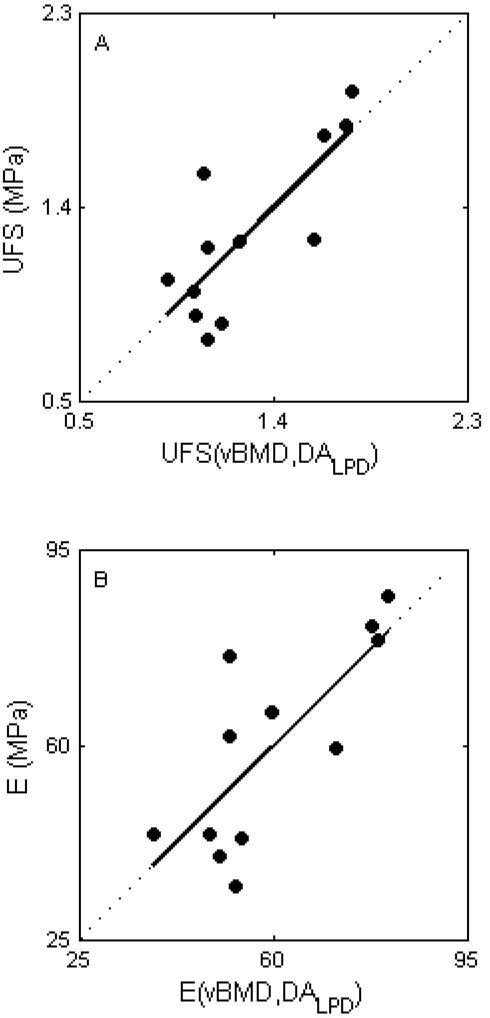

Figure 7.10 Relationships between DXA (vBMD) and LPD based DA (DA_{LPD}) with A/S UFS and A/S E. [A] UFS(vBMD,DA_{LPD}) = 15.03(vBMD) + 1.42(DA_{LPD}) – 2.41 (n = 12, $r^2 = 0.62$ and $p < 0.05$); [B] E(vBMD,DA_{LPD}) = 582.02(vBMD) + 74.44(DA_{LPD}) – 115.96 (n = 12, $r^2 = 0.58$ and $p < 0.05$). Dotted lines represent lines of identity.

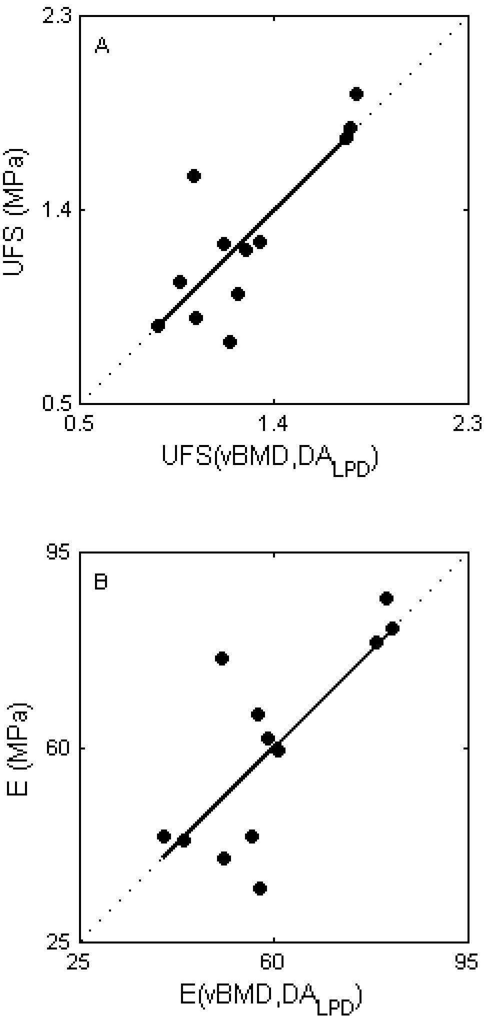

Figure 7.11 Relationships between BV/TV and LPD based DA (DA$_{LPD}$) with A/S UFS and A/S E. [A] UFS(BV/TV,DA$_{LPD}$) = 0.17(BV/TV) + 1.48(DA$_{LPD}$) – 3.06 ($n = 12$, $r^2 = 0.66$ and $p < 0.05$); [B] E(BV/TV,DA$_{LPD}$) = 6.13(BV/TV) + 76.71(DA$_{LPD}$) – 135.65 ($n = 12$, $r^2 = 0.57$ and $p < 0.05$). Dotted lines represent lines of identity.

The addition of architectural parameters did not significantly improve the amount of variance explained in $u_{A/S}$ over that explained by BV/TV or vBMD alone (Table 7.6). However, there was a trend toward significance ($p = 0.06$) with the addition of DA$_{LPD}$ to BV/TV in explaining the variance in $u_{A/S}$.

7.4 Discussion

In this study, measures of trabecular structural anisotropy and total surface were used in conjunction with measures of bone density to explain the variance in mechanical parameters following different loading modes. Differences in the relationship between structural anisotropy and mechanical parameters from first and second overload were used as an indication of structural change following overload. Results showed that the addition of structural anisotropy to bone density did not significantly improve the amount of variance explained in mechanical parameters from first overload in the SI direction. The addition of structural anisotropy to bone density did significantly improve the amount of variance explained in mechanical parameters from first overload in the AP direction. In second overloads, a complementary pattern was observed. Structural anisotropy significantly improved the amount of variance accounted for in mechanical parameters from SI overload following an initial AP overload (A/S), while no significant improvements were noted for mechanical parameters from AP overload following an initial SI overload (S/A). Though, undergoing similar loading modes, that is, AP elements likely underwent bending during SI compression and SI elements likely underwent bending during AP compression, these results that SI and AP elements of vertebral trabecular bone respond differently to compressive overload.

In first overload tests in the SI direction, the addition of structural anisotropy did not significantly improve the amount of variance explained in UFS, E and *u*, over BV/TV alone. A number of studies have demonstrated that for orthotropic structures, such as vertebral trabecular bone, the orthotropic mechanical properties are a function of volume fraction and fabric (4, 6, 10, 15, 20, 21), where fabric can be considered as the combined information of degree of anisotropy and direction of anisotropy (6, 8, 26). In first overload SI tests, the influence of fabric was negligible. This is due to the fact that the trabecular bone cubes used in this study were cut in their anatomical configuration and mechanically tested under monotonic compression in the direction corresponding to the principle orthotropic material direction. Since the principal orthotropic material direction closely corresponds to the principal (or maximum) fabric direction (22), the influence of fabric in this direction can be thought of as a scaling of mechanical parameters by a factor equal to unity. Deviations away from the principal orthotropic direction result in scaling factors less than unity. This was observed in first overload results for tests in the AP direction. In these tests, the addition of trabecular structural anisotropy improved the amount of variance explained in mechanical properties such as UFS and E over density based measures (BV/TV and vBMD) alone. Using information from vBMD and DA_{LPD}, up to 69% of the variance in UFS was accounted for. This was a 22% improvement over vBMD alone. Using BV/TV in place of vBMD, this result was improved by a further 12% to 81%. Thus, in the AP direction, structural anisotropy made a significant contribution to mechanical properties.

The novel aspects of the present study are the results from the second overloads carried out in the orthogonal direction to the initial overload. In S/A overload tests, apparent elastic modulus was 30% less than first overload AP mechanical tests (Chapter 4). Therefore, the apparent elastic orthotropic properties in the AP direction changed as a result of SI overload. While this study provides no direct evidence of a change in orthotropic structural symmetry in the AP direction, the changes in the univariate relationships between mechanical and architectural parameters, seen between AP and S/A tests (Chapter 4, Tables 4.5 and 4.6), indicate that SI overload changed the structural basis of the relationship in the AP direction. The addition of structural anisotropy did not make a significant contribution to this complex combination of changes in both elastic and structural orthotropic properties. BV/TV was the only parameter capable of explaining some of the mechanical variance in S/A tests.

This is contradictory to results of Liu *et al* (2003) (15), where orthotropic structural symmetry was not found to change following damage in the orthogonal direction. However, Liu *et al* (15) only tested bovine tibia models to less than 2% apparent compressive strain using finite element analyses. In the present study, human vertebral trabecular bone samples were overloaded in the orthogonal direction to 10% apparent strain. While damage from orthogonal strains less than 2% mays not affect orthotropic properties (15), the results here suggest that SI overload of vertebral trabecular bone alters AP structural properties.

AP overload did not significantly affect SI mechanical integrity (Chapter 4). However, results in the present study show a shift in the involvement of structural anisotropy compared to first overload in the SI direction. In second overload tests, DA_{LPD} improved the amount of variance explained in $UFS_{A/S}$ and $E_{A/S}$, with a trend toward significance for $u_{A/S}$ ($p = 0.06$). Since the orthotropic structural properties are a function of volume fraction and fabric (4-6, 10, 15, 26) and there was no change in BV/TV, one could speculate that the orthotropic structural symmetry must have changed to maintain SI mechanical integrity. While no direct evidence of this was available from the experiments carried out in this study, it is consistent with changes observed in the univariate relationship between SI and A/S mechanical and architectural parameters (Chapter 4, Tables 4.5 and 4.6).

These findings complement those found in a previous study (Chapter 4) and are supported by observations by other investigators. Liu *et al* (2003) (15) carried out finite element modelling on bovine tibial samples. Using an isotropic, perfectly damaging constitutive model, Liu *et al* simulated apparent damage by on-axis and transverse shear loading. They found no changes in orthotropic properties before and after damage, with the principal directions of the elasticity tensor and fabric tenor being aligned after damage. In their study, the largest change in the material co-ordinate system was caused by shear in an on-axis plane, however the change was largely confined to the transverse plane. Liu *et al* (2003) (15) concluded that following damage in the transverse plane, passive trabecular structural properties maintain the orientation of the principal elastic direction. This allows the trabecular structure to maintain most of its mechanical properties for normal loading conditions and gives a window of opportunity for the repair of structures orthogonal to the principal loading direction. Niebur *et al* (2002) (20) carried out biaxial failure experiments on bovine tibial trabecular bone samples. High resolution finite element models were used to determine the uniaxial and multiaxial yield properties for each sample. Their results indicated a difference between on-axis and transverse loading modes. They found that samples could be loaded off-axis beyond their yield point while maintaining structural integrity on-axis. This behaviour was deemed protective, allowing the structure to heal following damage sustained during off-axis or transverse overload. Wang *et al* (2006) (29) mechanically tested samples of bovine proximal tibia bone by compressive overload followed by torsional overload. In a subsequent study, Wang *et al* (29) mechanically tested similar bovine proximal tibia samples by torsional overload followed by compressive overload. In each study a number of microdamage variables were measured. In comparing the two studies, Wang *et al* concluded that the percentage of the original microcracks that propagated due to compressive overloading followed by torsional overloading were significantly greater than those from torsional overloading followed by compressive overloading (29).

Although the type of bone, modes and types of loading of the studies highlighted above differ from that of the present study, all provide insight into the underlying mechanisms of trabecular bone damage properties and further support the notion of differences between load bearing (longitudinal) and off-axis (transverse) trabecular elements. Combined with the conclusions presented in Chapter 4, the present study suggests that structural mechanisms allow the maintenance of mechanical integrity of trabecular elements in the principle orthotropic direction during traumatic events.

Given that trabecular bone is mechanically anisotropic (3, 9, 16-19), scalar measures of bone density (BV/TV or vBMD) cannot explain all of the mechanical properties trabecular bone (27).

Trabecular bone’s mechanical properties must be a function of bone density and architecture (4, 6, 10, 26). Thus, quantification of trabecular structural anisotropy may be of significance in clinical settings. This chapter indicates that the mechanical properties of vertebral trabecular bone can be accounted for using non-invasive, projection based methodologies. The projection based DA_{LPD} was the only parameter to make significant contributions to both first and second overload mechanical properties, though this could be partially attributed to the fact that DA_{LPD} was measured from the sagittal plane of trabecular bone cubes. This plane contains information about both SI and AP structures. $DA_{\mu CT}$ was a 3D measure that did not discriminate between transverse structures. Using PMIL and LPD combined with non-invasive modalities such as DXA and other X-ray based imaging techniques it is possible to gain insight into trabecular bone mechanical properties.

There are limitations to the study presented here. Structural anisotropy and total surface were only measured once, prior to initial overload. Thus, any changes to the trabecular structure following initial overload were not taken into account. Rather, differences in the relationship between structural anisotropy and mechanical parameters were used as an indication of structural change. Work by Keaveny *et al* (11, 13) suggests that the platen compression test has inherent systemic and random errors that contribute to underestimation of mechanical properties. The protocol presented by Keaveny *et al* includes embedding samples in brass endcaps. In the current investigation, each sample was tested twice, once in each of the two directions. This precludes the use of endcaps. Though the suggested protocol is of importance in determining absolute values, the systemic errors addressed by the protocol of Keaveny *et al* are not critical in the current study since relative differences were examined. DXA based vBMD did not correlate with BV/TV as well as was expected ($r^2 = 0.63$, $p < 0.01$). This was attributed to DXA sample scan size limitation, resolution and the bone segmentation algorithms used by the DXA machine. Improvements in non-invasive bone imaging would result in improved assessment of trabecular bone density. Consequently, multivariate models using µCT based BV/TV and projection based PMIL and LPD were tested. These analyses confirmed that with an accurate measure of the amount of bone (BV/TV) and the addition of structural anisotropy information from non-invasive measures such as the LPD, up to 81% of the variance in UFS and E could be explained. This was an improvement of approximately 30% over BV/TV alone.

In summary, this study has provided further evidence that vertebral trabecular bone is structured to maintain the integrity of the principle on-axis (load bearing) structure subsequent to trauma. Specifically, overload in the AP direction did not affect SI mechanical integrity. Furthermore, the structural anisotropy of the trabecular bone was found to be a significant contributor to its mechanical properties. Using techniques introduced in this thesis, it was possible to quantify trabecular structural anisotropy and improve the amount of variance accounted for in mechanical parameters. The implications of these findings are that measures of structural anisotropy have the potential to improve clinical assessment of trabecular bone.

References

1. Caldwell, C. B., Willett, K., Cuncins, A. V., and Hearn, T. C. Characterization of vertebral strength using digital radiographic analysis of bone structure. Med Phys 22*:*611-5; 1995.
2. Ciarelli, M. J., Goldstein, S. A., Kuhn, J. L., Cody, D. D., and Brown, M. B. Evaluation of orthogonal mechanical properties and density of human trabecular bone from the major metaphyseal regions with materials testing and computed tomography. J Orthop Res 9*:*674-82; 1991.
3. Ciarelli, T. E., Fyhrie, D. P., Schaffler, M. B., and Goldstein, S. A. Variations in three-dimensional cancellous bone architecture of the proximal femur in female hip fractures and in controls. J Bone Miner Res 15*:*32-40; 2000.
4. Cowin, S. C. The Relationship Between the Elasticity Tensor and the Fabric Tensor. Mechanics of Materials 4*:*137 - 147; 1985.
5. Cowin, S. C. Remarks on the paper entitled 'Fabric and elastic principal directions of cancellous bone are closely related'. J Biomech 30*:*1191-3; 1997.
6. Cowin, S. C., and Turner, C. H. On the relationship between the orthotropic Young's moduli and fabric. J Biomech 25*:*1493-4; 1992.
7. Currey, J. D. Bones - Structure and Mechanics. Princeton University Press; 2002.
8. Harrigan, T. P., and Mann, R. W. Characterization of Microsturctural Anisotropy in Orthotropic Materials Using a Second Rank Tensor. Journal of Material Science 19*:*761 - 767; 1984.
9. Homminga, J., McCreadie, B. R., Ciarelli, T. E., Weinans, H., Goldstein, S. A., and Huiskes, R. Cancellous bone mechanical properties from normals and patients with hip fractures differ on the structure level, not on the bone hard tissue level. Bone 30*:*759-64; 2002.
10. Kabel, J., van Rietbergen, B., Odgaard, A., and Huiskes, R. Constitutive relationships of fabric, density, and elastic properties in cancellous bone architecture. Bone 25*:*481-6; 1999.
11. Keaveny, T. M., and Hayes, W. C. A 20-year perspective on the mechanical properties of trabecular bone. J Biomech Eng 115*:*534-42; 1993.
12. Keaveny, T. M., Morgan, E. F., Niebur, G. L., and Yeh, O. C. Biomechanics of trabecular bone. Annu Rev Biomed Eng 3*:*307-33; 2001.
13. Keaveny, T. M., Pinilla, T. P., Crawford, R. P., Kopperdahl, D. L., and Lou, A. Systematic and random errors in compression testing of trabecular bone. J Orthop Res 15*:*101-10; 1997.
14. Ketcham, R. A., and Ryan, T. M. Quantification and Visualization of Anisotropy in Trabecular Bone. Journal Of Microscopy 213*:*158 - 171; 2004.
15. Liu, X., Wang, X., and Niebur, G. L. Effects of damage on the orthotropic material symmetry of bovine tibial trabecular bone. J Biomech 36*:*1753-9; 2003.
16. Mosekilde, L. Age-related changes in vertebral trabecular bone architecture--assessed by a new method. Bone 9*:*247-50; 1988.
17. Mosekilde, L. Normal vertebral body size and compressive strength: relations to age and to vertebral and iliac trabecular bone compressive strength. Bone 7*:*207-12; 1986.
18. Mosekilde, L., and Danielsen, C. C. Biomechanical competence of vertebral trabecular bone in relation to ash density and age in normal individuals. Bone 8*:*79-85; 1987.
19. Mosekilde, L., and Viidik, A. Correlation between the compressive strength of iliac and vertebral trabecular bone in normal individuals. Bone 6*:*291-5; 1985.
20. Niebur, G. L., Feldstein, M. J., and Keaveny, T. M. Biaxial failure behavior of bovine tibial trabecular bone. J Biomech Eng 124*:*699-705; 2002.
21. Niebur, G. L., Yuen, J. C., Burghardt, A. J., and Keaveny, T. M. Sensitivity of damage predictions to tissue level yield properties and apparent loading conditions. J Biomech 34*:*699-706; 2001.
22. Odgaard, A., Kabel, J., van Rietbergen, B., Dalstra, M., and Huiskes, R. Fabric and elastic principal directions of cancellous bone are closely related. J Biomech 30*:*487-95; 1997.
23. Rice, J. C., Cowin, S. C., and Bowman, J. A. On the dependence of the elasticity and strength of cancellous bone on apparent density. J Biomech 21*:*155-68; 1988.
24. Smit, T. H., Schneider, E., and Odgaard, A. Star length distribution: a volume-based concept for the characterization of structural anisotropy. J Microsc 191 (Pt 3)*:*249-57; 1998.
25. Turner, C. H. and Burr, D. B. Experimental Techniques for Bone Mechanics. In*:* S. C. Cowin (ed.), Bone Mechanics Handbook, pp. 7/1 - 7/35, CRC Press, 2001.
26. van Rietbergen, B. a. H., R. Elastic Constants of Cancellous Bone. In*:* S. C. Cowin (ed.), Bone Mechanics Handbook, pp. 15/1 - 15/24: CRC Press; 2001.
27. Waarsing, J. H., Day, J. S., and Weinans, H. Longitudinal micro-CT scans to evaluate bone architecture. J Musculoskelet Neuronal Interact 5*:*310-2; 2005.
28. Wang, X., Guyette, J., Liu, X., Roeder, R. K., and Niebur, G. L. Axial-shear interaction effects on microdamage in bovine tibial trabecular bone. Eur J Morphol 42*:*61-70; 2005.
29. Wang, X., and Niebur, G. L. Microdamage propagation in trabecular bone due to changes in loading mode. J Biomech 39*:*781-90; 2006.

Chapter Eight

Thesis Summary

Although there are now many studies describing empirical relationships between strength properties of bone and various explanatory variables, the need for improved non-invasive diagnostic techniques to assess bone fragility is at the core of importance in clinical problems such as osteoporosis. In addition to the assessment of structural characteristics, further understanding into the mechanics of trabecular bone is also needed. This thesis focused on gaining insight into some of the mechanical properties of trabecular bone and implementing strategies for the assessment of trabecular structural anisotropy from non-invasive x-ray (projection) based information.

In Chapter 4, fundamental relationships between SI and AP elements of vertebral trabecular bone where examined using a novel mechanical testing protocol. This study showed that SI overload affected the mechanical integrity of AP trabecular elements, while AP overload did not significantly affect the mechanical integrity of SI trabecular elements. Architectural analyses revealed that the structural bases of the relationship between mechanical properties and structural anisotropy changed following overload in the orthogonal direction. These findings were attributed to passive structural properties that maintain the integrity of the principle (SI) load bearing elements subsequent to trauma. In addition to these findings, results indicated that the mechanical anisotropy was a dominant feature of vertebral trabecular bone. The mechanical anisotropy remained a dominant feature, even after the trabecular structure was overloaded in the orthogonal direction, implicating its role in vertebral trabecular bone damage mechanics.

Using the knowledge that mechanical anisotropy is intimately related to the trabecular structural anisotropy (6), two novel techniques for assessing structural anisotropy from projections were presented. In chapter 5, the PMIL was introduced and some of its properties explored. It was found that the PMIL could measure structural anisotropy and total bone surface from projections of the structure. PMIL based measures were found to be highly correlated to MIL based measures of the same trabecular properties. In Chapter 6, the LPD was introduced and some of its properties explored. Following findings in the literature that the LFD, developed by Geraets *et al* (1-5), was more sensitive to structural anisotropy than the MIL (3), the LPD was developed to produce a projection based measure that was more sensitive to trabecular structural variations than the PMIL. LPD based measures were found to be equivalent to the LFD based measures.

The ability of these novel, projection based measures to contribute to explaining variance in mechanical properties was explored (Chapter 7). In the study presented in Chapter 7, results further supported previous findings (Chapter 4) that vertebral trabecular bone has passive properties that provide protective mechanisms to maintain the integrity of the principle load bearing structure subsequent to trauma. Results presented in Chapter 7 also suggest that the addition of structural anisotropy to bone density can significantly improve the assessment of trabecular mechanical properties. PMIL and LPD based measures, in combination with DXA based vBMD or µCT based BV/TV, significantly improved the assessment of trabecular mechanical properties.

The studies presented in this thesis have shown that the structural basis of vertebral body trabecular bone mechanical properties change with overload in the orthogonal direction. Information about trabecular structure can be extracted from projection based information and this information can improve the explanation of variance in trabecular bone mechanical properties. Collectively, these findings demonstrate the potential use of non-invasive methodologies in the assessment of trabecular bone and warrants further investigation into the use of such techniques for clinical use.

References

1. Geraets, W., and Van der Stelt, P. Analysis of the radiographic trabecular pattern. Pattern Recognition Letters 12*:*575-581; 1991.
2. Geraets, W., van Ruijven, L., Verheij, J., van Eijden, T., and van der Stelt, P. A sensitive method for measuring spatial orientation in bone structures. Dentomaxillofac Radiol 35*:*319-25; 2006.
3. Geraets, W. G. Comparison of two methods for measuring orientation. Bone 23*:*383-8; 1998.
4. Geraets, W. G., Van der Stelt, P. F., and Elders, P. J. The radiographic trabecular bone pattern during menopause. Bone 14*:*859-64; 1993.
5. Geraets, W. G., Van der Stelt, P. F., Lips, P., Elders, P. J., Van Ginkel, F. C., and Burger, E. H. Orientation of the trabecular pattern of the distal radius around the menopause. J Biomech 30*:*363-70; 1997.
6. Odgaard, A., Kabel, J., van Rietbergen, B., Dalstra, M., and Huiskes, R. Fabric and elastic principal directions of cancellous bone are closely related. J Biomech 30*:*487-95; 1997.